Diyala Journal of Engineering Sciences

Journal homepage: https://djes.info/index.php/djes

ISSN: 1999-8716 (Print); 2616-6909 (Online)

Numerical model of the steady-state condenser and effect of pressure drop correlations on refrigerant physical parameters

Ahmed Haidour[1*], Boumediene Touati[2] , Achour Mansouri[3] , Hamou Soualmi[3]

[1] Energetic Laboratory in Arid Zones, ENERGARID, Faculty of Technology, University TAHRI Mohamed, Bechar, Algeria
[2] Energetic Laboratory in Arid Zones, ENERGARID, Faculty of exact sciences, University TAHRI Mohamed, Bechar, Algeria
[3] Research Unit for Renewable Energies in Saharan region, URERMS, Renewable Energy Development Center, CDER, 01000 Adrar, Algeria

ARTICLE INFO

Article history:
Received: 29/06/2025.
Revised: 29/11/2025
Accepted: 15/01/2026,
Available online: 15/03/2026

Keywords:
Single-phase region
Two-phase region
Refrigerant/air condenser
Numerical simulation
Pressure drop
Steady-state

ABSTRACT

Air-cooled condensers are an important part of modern refrigeration systems because they affect how well the system works and how much energy it uses. This study develops an integrated numerical model to simulate the behaviour of an air-cooled condenser using Fortran and RefProp 8.0 to evaluate the thermophysical properties of R22 and R32 refrigerants. The model solves five equations at the same time. These include the Navier-Stokes equations for the main refrigerant's mass, momentum, and energy conservation, the energy balance equation for the condenser wall, and the enthalpy equation for the secondary fluid (air). Due to the nonlinear nature of the system, the full implicit Preismann scheme was applied in conjunction with the Newton-Raphson and bisection methods to improve numerical stability and accelerate convergence. The results demonstrate that the developed model precisely forecasts the steady-state performance of the condenser, offering thorough analyses of the pressure drop and heat transfer coefficients in both the single-phase and two-phase flow regions. The effective condenser length was found to be 20 meters for R22 refrigerant and 48 meters for R32, with the two-phase zone dominating by 96%, indicating that condensation occurs primarily within this section. Furthermore, the refrigerant behaves as an incompressible fluid in the partially cooled liquid zone. Comparison with EVAP-COND 4.0 and previous studies revealed a deviation of less than ±1% in the performance parameters. These results demonstrate the long-term promise of the developed model as an effective tool for designing and optimizing air-cooled condensers for industrial refrigeration and air conditioning applications.

1. INTRODUCTION

Refrigeration systems are essential in modern society due to their critical applications in air conditioning, food preservation, and industrial processes. They play a key role in maintaining the quality of perishable goods, optimizing manufacturing procedures, and ensuring comfort in both residential and commercial environments [1, 2]. These systems are particularly vital in healthcare, where they are used for the safe storage of vaccines and pharmaceuticals [3], and in the food industry, where they help minimize waste and enhance safety [4]. Air conditioning, an integral component of refrigeration technology, is especially important in regions experiencing rising temperatures due to climate change [5]. Furthermore, as the demand for energy-efficient refrigeration increases, these systems are closely linked to sustainability goals due to their significant impact on energy consumption and carbon emissions [6]. Therefore, improving condenser performance is crucial for enhancing overall system efficiency and reducing energy usage.

A typical refrigeration system consists of four main components: the compressor, condenser, thermal expansion valve (TEV), and evaporator (as shown in Figure 1). Among these, the condenser is of particular importance, as its primary function is to convert the high-pressure, high-temperature refrigerant vapor into a subcooled liquid, thereby rejecting heat for the surrounding environment along the flow path.

* Corresponding author's E-mail: haidour.ahmed@univ-bechar.dz
DOI: 10.24237/djes.2026.19101

This work is licensed under a Creative Commons Attribution 4.0 International License.

Inside the condenser, the refrigerant passes through three distinct thermodynamic regions:

- Single-phase gas region (superheated vapor): the refrigerant enters the condenser as a superheated gas.
- Two-phase region (liquid–vapor mixture): as the temperature decreases, the refrigerant gradually condenses into a mixture of liquid and vapor.
- Single-phase liquid region (subcooled liquid): the refrigerant exits the condenser as a subcooled liquid.

Temperature variations of the refrigerant directly influence its physical and thermodynamic properties, such as pressure, velocity, volumetric density, and viscosity. This study investigates and compares various correlations used to predict pressure drops in the condenser and examines their effects on these parameters. The simulations were initially conducted using R22; however, since this refrigerant is an ozone-depleting substance, an environmentally friendly alternative (R32) was also examined.

The main objective of this work is to predict the steady-state behavior of the condenser under specific operating conditions. Although the current model does not account for dynamic behavior or complex real-world conditions, it provides a valuable numerical framework for designers and engineers to enhance air-cooled condenser performance through adjustments to system inputs and geometric parameters.

The added value of this study lies in its numerical methodology, developed using Fortran, which is rarely employed in the literature due to its implementation complexity. Furthermore, the study presents a comparative analysis of various pressure-drop correlations and their influence on the thermophysical and hydrodynamic behavior of the refrigerant within the condenser, contributing to improved understanding and optimization of the refrigeration system design.

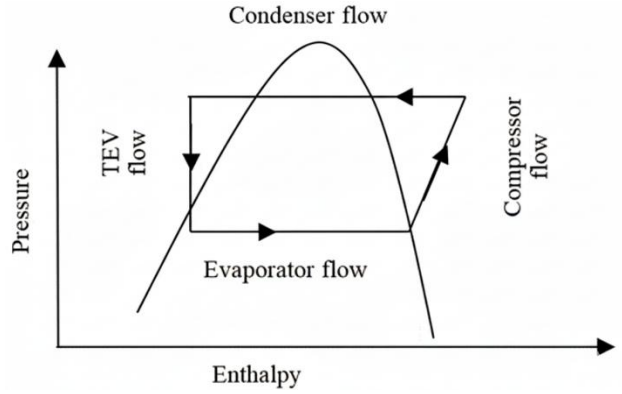

Figure 1. Mollier diagram of a cooling system [7].

2. LITERATURE REVIEW

Over the past three decades, numerous studies have examined the condensation heat transfer and pressure drop of refrigerants in mini- and micro-channels and compact heat exchangers to improve condenser performance and system efficiency.

2.1. Experimental Investigations

Yan and Lin [8] experimentally investigated the condensation of R134a in a small horizontal circular pipe that has an inside diameter of 2 mm. They found that the average heat transfer coefficient for condensation was approximately 10% higher than that in a pipe that has an inside diameter larger than 8 mm. They noticed that the coefficient went up when the heat fluxes were lower and the mass fluxes were higher. The pressure drop, on the other hand, went up when the mass flux was higher but down when the heat flux was higher. Liu and Li [9] also looked at the condensation of R32, R152a, and R22 in mini-channels with hydraulic diameters between 0.95 and 1.3 mm. They found that R32 acted like R22 but had pressure losses that were up to 15% lower. Among several empirical correlations tested, the Kim and Mudawar [10] model provided the best agreement with experimental data, with 73% of the data points falling within ±30% deviation. Kim and Mudawar [11] conducted a meta-analysis that aggregated a comprehensive database of 7115 experimental data points from 36 sources. They revealed that most existing correlations for frictional pressure drops in mini/microchannels had a mean absolute deviation exceeding 26%, motivating the development of new dimensionless-based predictive correlations. Del Col et al. [12] also looked into propane (R290) condensation in a 0.96 mm horizontal minichannel. They found local heat transfer coefficients between 7000 and 9500 W/m^2K for mass fluxes of $200 - 800\,kg/m^2s$ and pressure gradients of 10 to 25 kPa/m. This indicated that R290 could be a viable choice for compact, low-charge refrigeration systems.

2.2. Compact Heat Exchangers

Kuo et al. [13] reported that in vertical plate heat exchangers (PHEs) equipped with 60° chevron plates, both the heat transfer coefficient for condensation and the frictional pressure drop increased almost linearly with vapor quality, and that increasing the imposed heat flux from 10 to 25 kW/m^2 enhanced the condensation performance by 30–40%. In contrast, Eldeeb et al. [14] reviewed available correlations for two-phase flow in PHEs. They found that most existing models exhibited deviations of up to ±50%, depending on the refrigerant type and plate geometry. Later, Tao et al. [15] validated and expanded the experimental database for PHEs and confirmed that

the Longo et al. correlation provided the most accurate heat transfer predictions, while 87% of the frictional pressure drop data were predicted within ±50% deviation, highlighting the persistent limitations of existing models for complex corrugated geometries.

Marzouk et al. [16] recently studied six helical tube heat exchanger configurations (HTHE1–HTHE6) with Reynolds numbers ranging from 16000 to 25000. They discovered that the HTHE6 two-pass configuration enhanced the overall heat transfer coefficient by approximately 125–185% in comparison to a uniform tube distribution. As the Reynolds number went up, the pressure drop got bigger. HTHE1 had the biggest drop. But HTHE6 had the best overall performance because it had the best exergy efficiency and the highest coefficient of performance. These results show that moving the tubes around can greatly improve heat transfer with only a small increase in the power needed to pump.

2.3. Numerical and CFD-Based Models

Wang et al. [17] developed a distributed dynamic model capable of predicting key system parameters, such as the coefficient of performance (COP), superheating, and subcooling, achieving excellent agreement with experiments with deviations below ±5%. Building on numerical modeling advancements, Fayssal and Moukalled [18] introduced a fully implicit coupled solver that simultaneously solved the conservation equations of mass, momentum, and energy, attaining high numerical stability and successfully reproducing up to 96% of the experimentally observed condensation behavior. Complementarily, Zhang et al. [19] performed CFD simulations of R410A condensation using the Volume of Fluid (VOF) model, revealing that the local heat transfer coefficient increased by approximately 40% when transitioning from the superheated to the saturated condensation region, primarily due to the formation and growth of the liquid film along the pipe wall.

Huang et al. [20] utilized computational fluid dynamics (CFD) to examine vapor–liquid separation in liquid-separation condensers featuring multi-pass-orifice headers. Their findings indicated that significant fluid impact in the baseline design (Case 0) resulted in considerable vapor leakage through the orifices. They conducted an orthogonal study (Case 1–Case 11) and determined that separation efficiency (η) is predominantly influenced by orifice diameter, followed by position and quantity. They identified three $1.5\,mm$ diameter orifices, positioned at two-thirds of the header diameter (2D/3), as the optimal configuration. This arrangement achieved a maximum η of 51.9% in Case 11, which also resulted in a greater pressure difference and a more uniform flow distribution. Li and Ju [21] conducted a related CFD study that integrated the VOF multiphase model with the Lee phase-change model to examine low-temperature condensation of various refrigerants outside a horizontal tube in LNG intermediate fluid vaporizers, achieving favorable correlation with experimental results across a broad spectrum of wall subcooling. Their findings indicated a maximum in the periodic-averaged heat transfer coefficient relative to saturation temperature (at $10\,°C$ subcooling, with corresponding saturation pressures of $0.35 - 0.65\,MPa$ for four refrigerants), underscored the advantageous effect of surface tension in reducing the condensate film thickness, and recognized dimethyl ether (DME) and butane as viable intermediate fluids for forthcoming IFV designs.

2.4. Recent Developments

Moradkhani et al. [22] compiled an extensive database of 8037 experimental data points covering 23 working fluids. They used artificial intelligence-based regression models like Multilayer Perceptron (MLP), Gaussian Process Regression (GPR), and Radial Basis Function (RBF) to guess how much pressure would drop due to friction during condensation. Among these, the GPR model demonstrated the highest predictive accuracy, achieving an Average Absolute Relative Error (AARE) of 4.1% and a coefficient of determination (R^2) of 99.23%, thereby outperforming all conventional empirical correlations. Sun et al. [23] also looked into the condensation of liquid methane in mini-pipes that were coming together. They found that the overall heat transfer performance improved by 94.7% compared to straight pipes, primarily due to enhanced turbulence intensity and the formation of thinner condensate films, which points to the possibility of geometric optimization for heat transfer enhancement in cryogenic applications.

Marzouk [24] employed Cantera–Python to investigate a steam Rankine cycle with water/steam at $50\,bar$ and $600\,°C$, while adjusting the condenser pressure from 0.78125 to $200\,kPa$ around a $12.5\,kPa$ baseline. Input heat, net work, and efficiency exhibited logarithmic declines with rising condenser pressure, while turbine-exit steam quality demonstrated a power-law increase, illustrating the trade-off between elevated efficiency at reduced condenser pressure and enhanced dryness at increased pressure.

Jiang et al. [25] enhanced a scroll expander for small organic Rankine cycles through experiments, 3D transient computational fluid dynamics utilizing real-gas equations of state, and Box–Behnken response surface methodology applied to five working fluids. R245fa had the highest isentropic efficiency of any pure fluid (49.2%), but the 0.3R123/0.7R245fa

mixture had the most power (up to 2.43 kW, 17.8% more than pure fluids), with a minimum prediction error of 1.28%, which is a favorable guide for designing compact ORC expanders.

Previous research highlights several gaps, including the absence of fully integrated numerical models that simultaneously capture thermal and hydrodynamic interactions in air-cooled condensers, the limited applicability of existing correlations to various refrigerants, and insufficient consideration of geometric and phase-distribution effects. Moreover, solving coupled Navier–Stokes and energy equations rarely utilizes high-performance computing tools like Fortran. Accordingly, this study develops a comprehensive Fortran-based model using Refprop 8.0 to simulate the steady-state behavior of air-cooled condensers with R22 and R32 refrigerants, aiming to enhance design optimization and promote eco-efficient performance.

3. GOVERNING EQUATIONS

A comprehensive simulation model was developed to analyze the performance of the cooling condenser, grounded in the fundamental principles of heat and mass transfer among the primary refrigerant, secondary refrigerant, and the condenser wall, as well as the thermodynamic relations governing the system's behavior. The implementation of this model presents a significant level of complexity due to the interaction of multiple coupled physical phenomena, particularly within the two-phase flow region. Consequently, the model was formulated under a series of simplifying assumptions, as detailed below.

- The refrigerant's physical properties only change in the direction of the flow, which means that it is one-way.
- Heat exchanges through conduction and radiation between the studied pipe and adjacent pipes are considered negligible.
- The flow in the two-phase region is assumed to be homogeneous, meaning the liquid and gas phases have equal velocities.
- The humidity is assumed to be zero, indicating that the surrounding air is completely dry.
- The inner diameter of the condenser pipe is constant.
- The fin's temperature matches the pipe's outer wall temperature.
- The refrigerant is compressible in all three regions of the condenser.

Based on these assumptions, this model is presented in Figure 2.

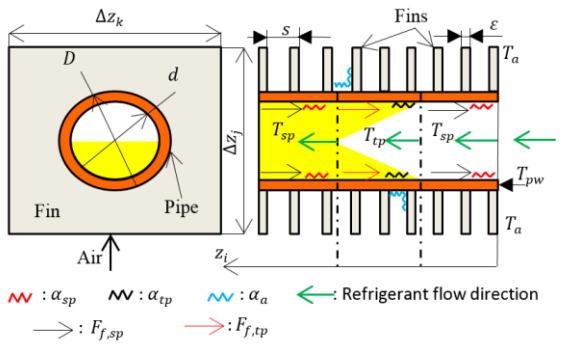

Figure 2. Finned pipe condenser model [26, 27].

These simplifying assumptions reduce the mathematical complexity of the model and facilitate its numerical solution, but they also restrict its reliability to a specific operating envelope. The one-dimensional, steady formulation neglects circumferential and entrance-region gradients, non-uniform air-side heating, and header-induced maldistribution, which can lead to an overestimation of heat transfer and the omission of localized pressure losses. Neglecting inter-tube conduction and thermal radiation is reasonable for moderate temperature differences and limited coil packing; however, for multi-row coils, mutual emission/absorption and thermal shadowing can alter the field uniformity, making this assumption non-conservative. The homogeneous two-phase model (slip = 1) suppresses phase-separation phenomena; in annular or intermittent regimes, substantial liquid–vapor slip typically biases frictional pressure losses, heat-transfer coefficients, the predicted two-phase length, and the axial location of extrema. Assuming dry air excludes fin-side condensation, additional external thermal resistances, and latent heat transfer, under humid conditions, the model therefore overpredicts thermal performance and ignores wet-coil effects on both convection and pressure drop. The assumption of a constant inner diameter, together with the omission of roughness evolution, fouling, and oil films, removes realistic dispersion mechanisms that increase pressure losses and reduce heat transfer over time. Equating the fin temperature with the outer tube-wall temperature implies unit fin efficiency, which is generally optimistic. Finally, treating compressibility effects as important in the superheated-vapor and two-phase regions but negligible in the subcooled-liquid region is valid for low-Mach flows with moderate pressure differences; near compressor discharge or at higher Δp, pressure–temperature coupling may modify the saturation-temperature distribution and the slope of the thermal curves.

3.1. Single-phase region

This model is governed by five fundamental equations: the mass conservation equation (equation

(1)) [17, 27, 28], the momentum conservation equation (equation (2)) [26, 28, 29], the energy conservation equation (equation (3)) [10, 30], the energy equation applied to the pipe wall (equation (4)) [26, 31], and the dry air enthalpy equation (equation (5)) [26].

3.1.1. Mass conservation equation

In a homogeneous, one-dimensional system, considering flow through a pipe of constant internal diameter and in the absence of internal sources of mass or energy, the continuity equation represents the conservation of mass within a control volume and its transport along the flow direction within the pipe. Under these conditions, it can be expressed as follows [17, 27, 28]:

$$\frac{\partial \rho_{sp}}{\partial t} + \frac{\partial (\rho_{sp} u)}{\partial z} = 0 \quad (1)$$

3.1.2. Momentum conservation equation

This equation represents the momentum balance (force equilibrium) for the fluid, where the pressure force, gravitational force (weight), and frictional force collectively contribute to the rate of change in momentum within the flow. Assuming a homogeneous and horizontal flow, the equation can be expressed as [26, 28, 29]:

$$\frac{\partial (\rho_{sp} u)}{\partial t} + \frac{\partial (\rho_{sp} u^2 + P)}{\partial z} + F_{f,sp} = 0 \quad (2)$$

3.1.3. Energy conservation equation

This equation shows the energy balance in the condenser. It shows that when the vapor condenses, its thermal content decreases, which causes heat to move to the pipe wall and then to the outside cooling medium (air). In other words, the wall and the secondary refrigerant gain the same amount of heat as the condensing vapor loses, which keeps the system's energy use low. For a one-dimensional, homogeneous flow in a pipe of constant inner diameter, the energy equation can be expressed as [10, 30]:

$$\frac{\partial (\rho_{sp} h_{sp})}{\partial t} + \frac{\partial (\rho_{sp} u h_{sp})}{\partial z} + \frac{4\alpha_{sp}(T_{pw} - T_r)}{d} = 0 \quad (3)$$

3.1.4. Energy equation applied to the pipe wall

This equation represents the energy balance within the metallic wall of the condenser pipe, indicating that the rate of temporal change in the wall's internal energy equals the net heat flux entering and leaving the wall. Assuming that heat transfer from the primary refrigerant to the ambient air occurs solely by convection through the condenser wall and that the outer wall temperature of the pipe is equal to the fin temperature, the equation can be expressed as [26, 31]:

$$c_{p,pw} M_{pw} \frac{\partial T_{pw}}{\partial t} - \pi d \Delta z_i \alpha_{sp} (T_{pw} - T_r) - \eta_A A_o \Delta z_i \alpha_a (T_{pw} - T_a) = 0 \quad (4)$$

3.1.5. Dry air enthalpy equation

This equation states that the heat lost by the condenser wall is equal to the heat gained by the air flowing across it, thereby ensuring the thermal energy balance on the air side of the condenser. Assuming that the air is completely dry, the equation can be expressed as [26]:

$$\frac{d(\dot{M}_a c_{p,a} T_a)}{dz_k} - \frac{\eta_A A_o \Delta z_i \alpha_a (T_{pw} - T_a)}{\Delta z_k} = 0 \quad (5)$$

3.2. Two-phase region

This model of the two-phase region is also governed by five equations:

- Mass conservation equation (equation (10)) [17, 27, 32].
- Momentum conservation equation (equation (25)) [26, 29, 32].
- Energy conservation equation (equation (29)) [10, 30, 32].
- Energy equation applied to the pipe wall (equation (30)) [26, 31].
- Formula for dry air enthalpy (equation (5)), which remains identical in both the two-phase and single-phase regions [26].

3.2.1. Mass conservation equation

Applying the mass conservation law for both vapor and liquid phases on a small pipe section yields [17, 27, 32]:

$$\frac{\partial (\psi \rho_g)}{\partial t} + \frac{\partial (\psi \rho_g u_g)}{\partial z} = \Gamma_{gl} \quad (6)$$

$$\frac{\partial}{\partial t}[\rho_l (1 - \psi)] + \frac{\partial}{\partial z}[\rho_l u_l (1 - \psi)] = \Gamma_{lg} \quad (7)$$

The mass flow per unit volume from liquid to gas is considered negative [32].

$$\Gamma_{lg} = -\Gamma_{gl} \quad (8)$$

By adding the two equations (6) and (7), the following equation is written:

$$\frac{\partial}{\partial t}\left[\psi \rho_g + \rho_l (1 - \psi)\right] + \frac{\partial}{\partial z}\left[\psi \rho_g u_g + \rho_l u_l (1 - \psi)\right] = 0 \quad (9)$$

By substituting the two equations (54) and (55) into equation (9), formula (10).is extracted.

$$\frac{\partial \rho_{tp}}{\partial t} + \frac{\partial (\rho_{tp} u)}{\partial z} = 0 \quad (10)$$

3.2.2. Momentum conservation equation

The momentum equations for both vapor and liquid phases are [26, 29, 32]:

$$\frac{\partial(\psi\rho_g u_g)}{\partial t}+\frac{\partial(\psi\rho_g u_g^2)}{\partial z}=-\frac{\partial(\psi P)}{\partial z}-F_{f,Igl}-F_{f,g,pw}+F_{gI} \quad (11)$$

$$\frac{\partial[(1-\psi)\rho_l u_l]}{\partial t}+\frac{\partial[(1-\psi)\rho_l u_l^2]}{\partial z}=-\frac{\partial[(1-\psi)P]}{\partial z}-F_{f,Ilg}-F_{f,l,pw}+F_{lI} \quad (12)$$

Adding equations (11) and (12):

$$\frac{\partial[\psi\rho_g u_g+(1-\psi)\rho_l u_l]}{\partial t}+\frac{\partial[\psi\rho_g u_g^2+(1-\psi)\rho_l u_l^2]}{\partial z}=-\frac{\partial P}{\partial z}-\left(F_{f,Igl}+F_{f,Ilg}\right)-\left(F_{f,g,pw}+F_{f,l,pw}\right)+\left(F_{gI}+F_{lI}\right) \quad (13)$$

The forces resulting from interfacial friction between the liquid and vapor phases in a steady state are evaluated according to the correlations provided in reference [33]:

$$F_{f,Igl}=-F_{f,Ilg}=\frac{3\xi_{fI}\psi^{0.5}\rho_g}{d}\left(u_g-u_l\right)\left|u_g-u_l\right| \quad (14)$$

The correlation for the friction factor between phases is expressed as follows [33]:

$$\xi_{fI}=0.005[1+75(1-\psi)] \quad (15)$$

In addition, the interfacial momentum transfer F_{gI} and F_{lI} due to mass transfer can be determined using equations (16) and (17). When gas is condensing, its velocity changes from u_g to u_l, and these terms describe the force associated with this velocity change. Wallis [34] has shown that for a reversible flow, the coefficient δ is 0.5.

$$F_{gI}=-\delta\Gamma_{gl}\left(u_g-u_l\right) \quad (16)$$

$$F_{lI}=-(1-\delta)\Gamma_{lg}\left(u_l-u_g\right) \quad (17)$$

The resultant of the frictional forces between the wall and the two phases is given by the following expression [26, 35]:

$$F_{f,tp}=F_{f,g,pw}+F_{f,l,pw} \quad (18)$$

The friction between the vapor phase flow and the inner wall of the pipe is minimal thanks to the utilization of special techniques in pipe design and the materials used in its manufacturing. In this state, the vapor phase flow is annular [26, 35].

$$F_{f,g,pw}=0 \quad (19)$$

Equation (18) can be written according to the formula:

$$F_{f,tp}=F_{f,l,pw} \quad (20)$$

In equation (13), the second term on the left side can be written as

$$\psi\rho_g u_g^2+(1-\psi)\rho_l u_l^2=\frac{\psi^2\rho_g^2 u_g^2}{\psi\rho_g}+\frac{(1-\psi)^2\rho_l^2 u_l^2}{(1-\psi)\rho_l}=\frac{\psi^2 G^2}{\psi\rho_g}+\frac{(1-\psi)^2 G^2}{(1-\psi)\rho_l}=\frac{x^2 G^2}{\psi\rho_g}+\frac{(1-x)^2 G^2}{(1-\psi)\rho_l} \quad (21)$$

By using the equations (54) and (55):

$$G^2=\rho_{tp}^2 u^2=\left[\psi\rho_g+(1-\psi)\rho_l\right]\rho_{tp}u^2 \quad (22)$$

To substitute equation (22) into equation (21):

$$\psi\rho_g u_g^2+(1-\psi)\rho_l u_l^2=\rho_{tp}u^2\left\{x^2\left[1+\frac{(1-\psi)\rho_l}{\psi\rho_g}\right]+(1-x)^2\left[1+\frac{\psi\rho_g}{(1-\psi)\rho_l}\right]\right\} \quad (23)$$

Equation (23) can be written as follows:

$$\psi\rho_g u_g^2+(1-\psi)\rho_l u_l^2=B\rho_{tp}u^2 \quad (24)$$

Where
Equation (58) defines B.
By substituting equations (14), (19), (20), (24), (54) and (55) into equation (13), equation (25) is written in the form:

$$\frac{\partial(\rho_{tp}u)}{\partial t}+\frac{\partial(B\rho_{tp}u^2+P)}{\partial z}+F_{f,tp}=0 \quad (25)$$

3.2.3. Energy conservation equation

Neglecting the change in kinetic and potential energy, the energy equation applied to an unsteady two-phase flow in a small section of the pipe is expressed as follows [9, 10, 30]:

$$\frac{\partial}{\partial t}\left[\psi\rho_g h_g+(1-\psi)\rho_l h_l\right]+\frac{\partial}{\partial z}\left[\psi\rho_g u_g h_g+(1-\psi)\rho_l u_l h_l\right]=\frac{4\alpha_{tp}(T_{pw}-T_r)}{d} \quad (26)$$

The two expressions on the left side of the equation can be simplified as follows:

$$\psi\rho_g h_g+(1-\psi)\rho_l h_l=\frac{u_g}{u_g}\psi\rho_g h_g+\frac{u_l}{u_l}(1-\psi)\rho_l h_l=\frac{G}{u_g}\psi h_g+\frac{G}{u_l}(1-\psi)h_l=\frac{G}{u}\left(\psi h_g+(1-\psi)h_l\right)=\rho_{tp}h_{tp} \quad (27)$$

$$\psi\rho_g u_g h_g+(1-\psi)\rho_l u_l h_l=G\psi h_g+G(1-\psi)h_l=G\left(\psi h_g+(1-\psi)h_l\right)=\rho_{tp}uh_{tp} \quad (28)$$

By substituting equations (27) and (28) into equation (26), formula (29) is written:

$$\frac{\partial(\rho_{tp}h_{tp})}{\partial t}+\frac{\partial(\rho_{tp}uh_{tp})}{\partial z}+\frac{4\alpha_{tp}(T_{pw}-T_r)}{d}=0 \quad (29)$$

3.2.4. Energy equation applied to the pipe wall

The equation for the energy applied to the pipe wall is written in the following formula [26, 31]:

$$c_{p,pw}M_{pw}\frac{\partial T_{pw}}{\partial t} - \pi d\Delta z_i \alpha_{tp}(T_{pw} - T_r) - \eta_A A_o \Delta z_i \alpha_a (T_{pw} - T_a) = 0 \quad (30)$$

4. DISCRETIZATION EQUATIONS

In this study, a fully implicit four-point Preismann (box-type) scheme is employed for the numerical solution of the governing equations along the condenser tube. The flow domain is divided into control volumes, and the governing conservation equations for mass, momentum, and energy are integrated over each control volume. These equations are discretized using a box-type stencil in the axial direction, with the unknown variable's values at adjacent spatial positions i and $i+1$ (see Figure 3).

For a variable $\phi\,(z)$ (e.g., density or friction force), the spatial derivative and the control-volume average can be expressed as follows [36]:

$$\frac{\partial \phi}{\partial z} = a_z \frac{\phi_{i+1}^{j+1} - \phi_i^{j+1}}{\Delta z} + (1 - a_z)\frac{\phi_{i+1}^{j} - \phi_i^{j}}{\Delta z} + O(\Delta z|0.5 - a_z| + \Delta z^2) \quad (31)$$

$$\phi_m = a_z \frac{\phi_{i+1}^{j+1} + \phi_i^{j+1}}{2} + (1 - a_z)\frac{\phi_{i+1}^{j} + \phi_i^{j}}{2} + O(\Delta z|0.5 - a_z| + \Delta z^2) \quad (32)$$

Here, ϕ_m is the average value of the variable in the control volume, and a_z is the weighting parameter used for the spatial discretization. In the present model, a fully implicit formulation is adopted by setting a_z=1, ensuring strict conservation of mass, momentum, and energy across the control volumes. Because the governing equations are solved in steady-state form, the numerical scheme does not require any time-marching procedure; therefore, no CFL-type or Δt-based stability constraints exist. The fully implicit Preismann scheme ($a_z = 1$) is unconditionally stable for one-dimensional convection–diffusion systems and guarantees strict conservation properties. The truncation-error expressions in Eqs. (31)–(32) confirm that the spatial discretization achieves second-order accuracy for sufficiently smooth fields.

4.1. Reason for Selecting the Preismann Scheme Computationally

The Preismann Scheme was adopted because it provides a robust and conservative approach for discretizing the governing equations of the condenser while preserving the physical balance of energy and mass within each control volume along the pipe. The Preismann method differs from traditional numerical methods like Euler or Crank–Nicolson because it directly accounts for the physical conservation laws. The flow domain is divided into small control volumes, each of which conserves mass, momentum, and energy.

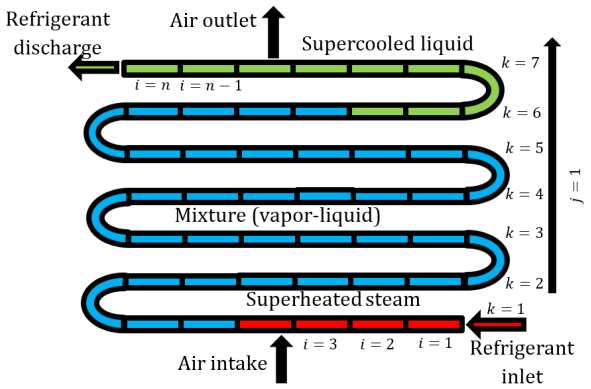

Figure 3. Condenser pipe segmentation into elemental nods [27].

4.2. Bisection method

When a function crosses through zero, its sign changes, which is the foundation of the bisection method's concept. The following program can be used to express the method [17]:

To find a root of $\phi(z) = 0$ in the interval of (a_0, b_0)

With which $\phi(a_0)\phi(b_0) < 0$

Pick tolerance ε

$Z_{i+1} = (a_i + b_i)/2 \quad , \quad i = 0,1,2,3, \ldots$

If $(|\phi(z_{i+1}) < \varepsilon|)$ root found, stop iteration.

Else

If $(\phi(z_{i+1})\phi(b_i) < 0) \;\; a_{i+1} = z_{i+1} \;;\; b_{i+1} = b_i$

Else $a_{i+1} = a_i \;;\; b_{i+1} = z_{i+1}$

End if

End if

4.3. Newton-Raphson method

The Newton-Raphson method uses the point where the tangent line crosses the zero axis as the next approximation. By calculating the slope of the function (the tangent) at the current estimate, the method iteratively updates the reference point until it converges to the root [17].

To find a root of $\phi(z) = 0$ with the initial guess z_0.

$$z_{i+1} = z_i - \frac{\phi(z_i)}{\phi'(z_i)} \quad , \quad i = 0,1,2,3, \ldots$$

In this study, the governing equations for the three phases within the condenser were solved entirely using the Newton-Raphson method, employing successive approximations and iterative updates to achieve convergence. The nonlinear system is solved by applying the damped Newton-Raphson algorithm with a consistent Jacobian matrix, ensuring thermodynamic equilibrium at each iteration.

To improve accuracy, the bisection method was used to calculate the mean temperatures of the refrigerant, the air, and the condenser pipe wall. This step improves the precision of the temperature profiles, which are critical for predicting the system's performance under steady-state conditions.

Figure 4 presents a general flowchart of the numerical algorithm used to solve for the variables in a heat exchanger system, including the refrigerant, air, and pipe wall sides.

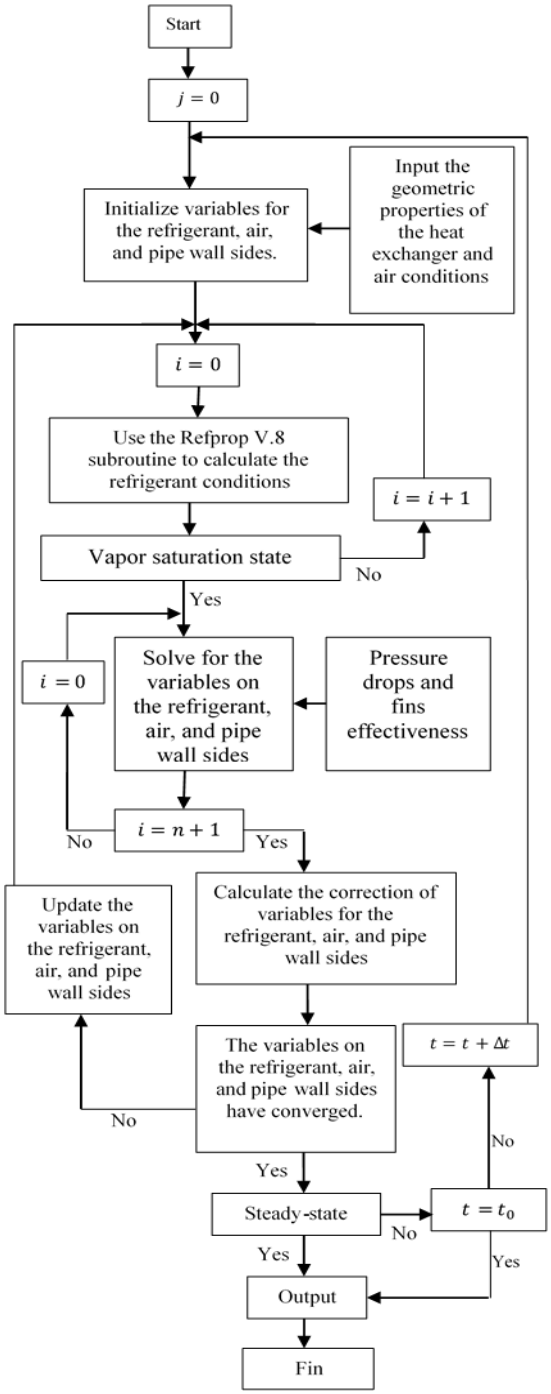

Figure 4. Flowchart of the numerical algorithm.

4.4. Advantages of the Newton–Raphson Method

The strong coupling among the mass, energy, and phase-change equations necessitates the use of the Newton-Raphson method with a consistent Jacobian matrix. This approach enforces thermodynamic equilibrium constraints at each iteration and achieves local quadratic convergence, meaning that the error decreases rapidly with each successive step. Consequently, the number of linear system solves is reduced, effectively compensating for the computational expense associated with Jacobian assembly.

In contrast, the Picard iteration method relies on decoupling and relaxation techniques, leading only to linear convergence. As the degree of nonlinearity increases, the number of required iterations grows significantly, reducing overall efficiency. Quasi-Newton schemes, such as Broyden's method, mitigate the overhead of derivative computation but may compromise robustness. They also exhibit greater sensitivity to damping parameters and line-search strategies, particularly in phase-change problems where stability is critical.

Therefore, the damped Newton-Raphson method is generally preferred for solving this class of nonlinear coupled systems, as it provides an optimal balance between convergence speed, robustness, and computational efficiency.

Despite these modeling limitations, the credibility of the present model remains high within the examined operating range. Numerical reliability was established through a mesh-sensitivity study, which indicated that the predicted thermal fields and total pressure drop remained stable and essentially grid-independent within the reported accuracy bounds. In addition, strict convergence criteria were enforced: the normalized updates of the primary variables ρ, u, T_r, T_a and T_{pw} were required to remain below (10^{-2}); and the nonlinear residuals of the five governing equations—mass, momentum, refrigerant energy, wall energy, and air enthalpy—were reduced below (10^{-10}, 10^{-6}, $10^{-5}, 10^{-10}, 10^{-10}$), respectively. A fully implicit steady-state solution procedure was adopted, which provides robust convergence behavior without altering the final converged solution.

To assess spatial and temporal discretization errors, a grid-independence study was carried out using three uniform axial meshes, denoted N1 (coarse), N2 (medium), and N3 (fine). For each mesh, the total heat transfer rate Q, the pressure drop ΔP, and the two-phase length L were monitored. The relative differences between the medium and fine grids (N2 ↔ N3) remained below 1–2% for all quantities, indicating that the solutions are effectively grid independent. In addition, a brief Richardson/GCI-style analysis was performed, and a time-step sensitivity test (Δt versus Δt/2) confirmed that temporal discretization errors are negligible compared with the spatial discretization error.

5. STEADY-STATE SYSTEM

A transient system is a time-dependent state in which the physical and thermodynamic properties vary with

time at a fixed location. In this case, the conservation laws include storage terms for mass, momentum, and energy, together with the thermal capacities of the wall and fins. Boundary conditions such as refrigerant flow rate, air temperature and humidity, and fan speed may vary with time. Start-up, shutdown, and load steps are typical examples; the steady solution is the equilibrium approached once the inputs become constant.

In a steady-state condenser, the refrigerant's thermophysical fields are time-invariant at a fixed location even while heat transfer and phase change continue. The mass flow rate is conserved along the circuit without leakage, whereas pressure and temperature may vary along the axis because of frictional losses and heat exchange. [37].

5.1. Single-phase region

The system can be written using equations (1) to (5) as follows:

$$\frac{\partial(\rho_{sp}u)}{\partial z} = 0 \tag{33}$$

$$\frac{\partial(\rho_{sp}u^2+P)}{\partial z} + F_{f,sp} = 0 \tag{34}$$

$$\frac{\partial(\rho_{sp}uh_{sp})}{\partial z} + \frac{4\alpha_{sp}(T_{pw}-T_r)}{d} = 0 \tag{35}$$

$$c_{p,pw}M_{pw}\frac{\partial T_{pw}}{\partial t} - \pi d\Delta z_i\alpha_{sp}\left(T_{pw}-T_r\right) - \eta_A A_o\Delta z_i\alpha_a\left(T_{pw}-T_a\right) = 0 \tag{36}$$

$$\frac{d(\dot{M}_a c_{p,a}T_a)}{dz_k} - \frac{\eta_A A_o\Delta z_i\alpha_a(T_{pw}-T_a)}{\Delta z_k} = 0 \tag{37}$$

Based on equations (31) and (32), the system is written as follows:

$$\frac{(\rho_{sp}u)_{i+1}^{j+1}-(\rho_{sp}u)_i^{j+1}}{\Delta z_i} = 0 \tag{38}$$

$$\frac{(\rho_{sp}uu)_{i+1}^{j+1}-(\rho_{sp}uu)_i^{j+1}}{\Delta z_i} + \frac{(P)_{i+1}^{1}-(P)_i^{j+1}}{\Delta z_i} + \frac{F_{f,sp,i+1}^{j+1}+F_{f,sp,i}^{j+1}}{2} = 0 \tag{39}$$

$$\frac{(\rho_{sp}uh_{sp})_{i+1}^{j+1}-(\rho_{sp}uh_{sp})_i^{j+1}}{\Delta z_i} - \frac{4}{d}\alpha_{sp,i}^{j+1}\left(T_{pw,i}^{j+1}-T_{r,i}^{j+1}\right) = 0 \tag{40}$$

$$T_{pw,i+1}^{j+1} - T_{pw,i+1}^{j} - \frac{\Delta t}{c_{p,pw}M_{pw}}\left[\pi d\Delta z_i\alpha_{sp,i}^{j+1}\left(T_{pw,i}^{j+1}-T_{r,i}^{j+1}\right) + \eta_A A_o\Delta z_i\alpha_{a,i}^{j+1}\left(T_{pw,i}^{j+1}-T_{a,i}^{j+1}\right)\right] = 0 \tag{41}$$

$$c_{p,a,i,j,k+1}^{j+1}T_{a,i,j,k+1}^{j+1} - c_{p,a,i,j,k}^{j+1}T_{a,i,j,k}^{j+1} - \frac{\eta_A A_o\Delta z_i\alpha_{a,i}^{j+1}}{\dot{M}_a}\left(T_{pw,i}^{j+1}-T_{a,i}^{j+1}\right) = 0 \tag{42}$$

5.2. Two-phase region

The system can be written using equations (10), (25), (29), (30), and (5) as follows:

$$\frac{\partial(\rho_{tp}u)}{\partial z} = 0 \tag{43}$$

$$\frac{\partial(B\rho_{tp}u^2+P)}{\partial z} + F_{f,tp} = 0 \tag{44}$$

$$\frac{\partial(\rho_{tp}uh_{tp})}{\partial z} + \frac{4\alpha_{tp}(T_{pw}-T_r)}{d} = 0 \tag{45}$$

$$c_{p,pw}M_{pw}\frac{\partial T_{pw}}{\partial t} - \pi d\Delta z_i\alpha_{tp}\left(T_{pw}-T_r\right) - \eta_A A_o\Delta z_i\alpha_a\left(T_{pw}-T_a\right) = 0 \tag{46}$$

The dry air enthalpy equation (equation (37)) remains the same in both the single-phase and two-phase regions.

Based on equations (31) and (32), the system is written as follows:

$$\frac{(\rho_{tp}u)_{i+1}^{j+1}-(\rho_{tp}u)_i^{j+1}}{\Delta z_i} = 0 \tag{47}$$

$$\frac{(B\rho_{tp}uu)_{i+1}^{j+1}-(B\rho_{tp}uu)_i^{j+1}}{\Delta z_i} + \frac{(P)_{i+1}^{j+1}-(P)_i^{j+1}}{\Delta z_i} + \frac{F_{f,tp,i+1}^{j+1}+F_{f,tp,i}^{j+1}}{2} = 0 \tag{48}$$

$$\frac{(\rho_{tp}uh_{tp})_{i+1}^{j+1}-(\rho_{tp}uh_{tp})_i^{j+1}}{\Delta z_i} - \frac{4}{d}\alpha_{tp,i}^{j+1}\left(T_{pw,i}^{j+1}-T_{r,i}^{j+1}\right) = 0 \tag{49}$$

$$T_{pw,i+1}^{j+1} - T_{pw,i+1}^{j} - \frac{\Delta t}{c_{p,pw}M_{pw}}\left[\pi d\Delta z_i\alpha_{tp,i}^{j+1}\left(T_{pw,i}^{j+1}-T_{r,i}^{j+1}\right) + \eta_A A_o\Delta z_i\alpha_{a,i}^{j+1}\left(T_{pw,i}^{j+1}-T_{a,i}^{j+1}\right)\right] = 0 \tag{50}$$

The dry air enthalpy equation (equation (42)) remains the same in both the single-phase and two-phase regions.

6. THE BOUNDARY CONDITIONS

Energy losses between the elements of the refrigeration system are ignored, and we assume that all physical parameters of the refrigeration at the condenser inlet are equal to those at the compressor outlet and all physical parameters of the refrigeration at the condenser outlet are equal to those at the thermal expansion valve inlet (Dirichlet conditions) [17, 31].

$Z = 0,$

$$\begin{Bmatrix}\rho, u, P, h,\\ T, G, \lambda, \mu,\\ c_p, \dot{M}_r, \dots\end{Bmatrix}_{\substack{Compressor\\ output}} = \begin{Bmatrix}\rho, u, P, h,\\ T, G, \lambda, \mu,\\ c_p, \dot{M}_r, \dots\end{Bmatrix}_{\substack{condenser\\ inlet}} \tag{51}$$

$Z = L,$

$$\begin{Bmatrix}\rho, u, P, h,\\ T, G, \lambda, \mu,\\ c_p, \dot{M}_r, \dots\end{Bmatrix}_{\substack{Condenser\\ outlet}} = \begin{Bmatrix}\rho, u, P, h,\\ T, G, \lambda, \mu,\\ c_p, \dot{M}_r, \dots\end{Bmatrix}_{\substack{TEV\\ inlet}} \tag{52}$$

For the internal boundaries, heat transfer occurs solely by convection between the refrigerant and the inner wall of the condenser tube. Continuity of both mass and energy is imposed at the interfacial surface separating the vapor and liquid phases.
Air is forced across the surface of the finned tubes, cooling the outer wall of the condenser. The air distribution across the surface is assumed to be uniform, assuming constant air velocity and incoming temperature. It is assumed that cooling is achieved by forced convection alone, without radiation or conduction in the environment.
The boundary conditions for the air at the inlet are defined as

$$h_a = h_{a,ambient} \quad (53)$$

The model also assumes that the air temperature and flow rate are constant at the inlet and that the heat transfer rates are uniform across the wall. The model assumes mass and energy continuity at the interface between the vapor and liquid phases. The outlet pressure of one region equals the inlet pressure of the other. This assumption leads to an inability of the model to predict accurately at the transition point, or its discontinuity, but it does not significantly affect the overall prediction of the refrigerant behavior inside the condenser.
Table 1 summarizes the boundary conditions and inlet parameters for this system.

Table 1: Boundary conditions and inlet parameters.

Parameter	Value		Unit
Refrigerant type	**R22**	**R32**	
Inlet temperature	30	30	$°C$
Inlet pressure	1191.9	1920	kPa
Mass flow rate	25	25	$kg\ h^{-1}$
Air inlet temperature	35	35	$°C$
Air velocity	3	3	$m\ s^{-1}$
Pipes thermal conductivity	389	389	$W\ m^{-1}K^{-1}$
Pipes specific heat	380	380	$J\ kg^{-1}K^{-1}$
Pipes density	8940	8940	$kg\ m^{-3}$
Fins thermal conductivity	200	200	$W\ m^{-1}K^{-1}$
Fins specific heat	860	860	$J\ kg^{-1}K^{-1}$
Fins density	2700	2700	$kg\ m^{-3}$

A refrigerant mass flow rate of $25\ kg\ h^{-1}$ was adopted for both R22 and R32, as reported in the table, in order to ensure a fair comparison between the two refrigerants under identical operating conditions. These conditions include an inlet temperature of $30°C$ and external air properties of $35°C$ and $3\ m\ s^{-1}$. This mass flow rate represents an appropriate value that enables effective internal convective heat transfer without causing an excessive pressure drop, especially considering the realistic condenser inlet pressures ($1191.9\ kPa$ for R22 and $1920\ kPa$ for R32). Moreover, this flow rate promotes a stable two-phase regime inside the condenser while maintaining refrigerant velocities within safe and practical operational limits.
From a geometrical and material standpoint, the tubes are assumed to be made of a highly conductive material (copper), with thermophysical properties of approximately $\lambda = 389\ W\ m^{-1}K^{-1}$, density $8940\ kg \cdot m^{-3}$, and specific heat $380\ J\ kg^{-1}K^{-1}$. Such properties minimize the thermal resistance between the refrigerant and the inner tube wall. The fins are assigned thermo-physical properties representative of aluminium ($\lambda = 200\ W\ m^{-1}K^{-1}$, density $2700\ kg \cdot m^{-3}$, and specific heat $860\ J\ kg^{-1}K^{-1}$), providing a large external heat transfer area with low structural weight, which is consistent with standard fin-and-tube condenser designs.
Additionally, forced convection is considered as the only heat transfer mechanism on the air side, with radiation and external conduction neglected. This assumption reflects standard testing conditions, which simplify the numerical model while still preserving a realistic representation of condenser operation.
Therefore, the selected mass flow rate and the thermo-physical properties of the tubes and fins establish a practical and efficient condenser configuration suitable for numerical simulation and allowing for a meaningful and reliable comparison between R22 and R32.

7. RESULTS And DISCUSSION

This model was developed based on the assumptions mentioned above. Table 2 presents the geometric characteristics of the heat exchanger shown in Figure 5. The simulation results generated numerical data, which were then converted into graphs, as illustrated in the following sections.

Table 2: Heat exchanger's geometric characteristics.

pipe length (m)	Number of rows	Number of lines
R22(30m), R32(50m)	1	R22(15), R32(25)
d (m)	***D (m)***	***ε (m)***
0.008	0.01	0.0003
s (m)	Δz_i ***(m)***	$\Delta z_k = \Delta z_j$ ***(m)***
0.0023	0.01	0.05

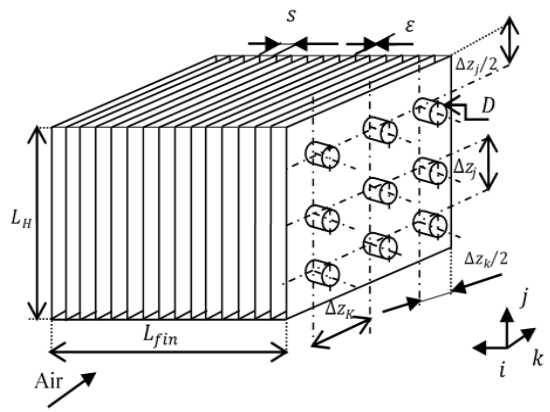

Figure 5. Compact heat exchanger schematic [27, 38].

Changing the parameters by $\pm 10\%$ can significantly impact the thermal system's efficiency. In the case of inlet temperature $30°C$, lowering the temperature to $27°C$ may increase thermal efficiency in some cases due to the refrigerant's increased ability to absorb heat, while raising the temperature to $33°C$ may decrease efficiency due to increased pressure and thermal resistance. For mass flow rate $25\ kg/h$, reducing it to $22.5\ kg/h$ may decrease the system's ability to absorb heat, weakening efficiency, while increasing it to $27.5\ kg/h$ may require additional energy to push the refrigerant through the system, thus increasing energy consumption. Changing the thermal conductivity of the pipes $389\ W/m\ K$ affects the pipe's ability to transfer heat; reducing the conductivity to 350 $W/m\ K$ may decrease system efficiency, while increasing it to $428\ W/m\ K$ could improve heat exchange. For other parameters, changing the pipe length ($30\ m$ for R22 and $50\ m$ for R32) will increase or decrease thermal resistance; shortening the length improves efficiency, while increasing it may increase thermal losses. Changing the number of rows, ranging from 13–17 rows for R22 and 22–28 rows for R32, will increase or decrease the heat exchange area; more rows improve efficiency, while reducing them decreases the heat exchange capability. Changing the roughness $0.0003\ m$ affects friction resistance; reducing the roughness to $0.00027\ m$ improves refrigerant flow inside the pipes and increases efficiency, while increasing it to $0.00033\ m$ may increase flow resistance and reduce efficiency. Changing the distance between pipes $0.0023\ m$ impacts heat exchange efficiency; reducing the distance improves exchange, while increasing it may decrease efficiency. Changing the vertical difference between pipes $0.01\ m$ can improve heat distribution when the difference is reduced, while increasing the difference may negatively impact heat distribution. Finally, changing the difference between rows $0.05\ m$ can improve heat distribution when the difference is reduced, while increasing it may hinder heat exchange.

Figure 6 illustrates a quasi-linear reduction in the pressure-enthalpy trend P(h) across the condenser as specific enthalpy decreases. At h=418.5kJ/kg, P for R22 decreases from 1.4269MPa to 1.4213MPa at h=243.1kJ/kg. The average slope of dP/dh=0.031kPa·kg/kJ (median local ≈ 0.036) and ΔP=6.1kPa over Δh=-175.4kJ/kg are the consequences of this. The curve for R32 decreases from roughly 521.4 to 266.7kJ/kg as h decreases from 2.2416 to 2.2289MPa. This result indicates that dP/dh is around 0.049kPa·kg/kJ (the median local is about 0.045) and ΔP is approximately 12.7 kPa over Δh, which is approximately -254.7 kJ/kg. The local behavior is consistent with the operation of condensers: as condensation proceeds and the liquid film thickens, interfacial slip decreases, wall-friction losses take over, and the P–h relation flattens; near the outlet, R22 exhibits minor nonlinearity when the incremental change in h becomes tiny, making differential ratios larger numerically; near the inlet (high h), rapid void-fraction evolution and acceleration effects increase dP/dh. In reality, for the same amount of heat evacuated in this range, R32 is more sensitive to variations in pressure than R22. Comparing the overall pressure drops to the absolute operating pressures of the condensers, they are still minimal.

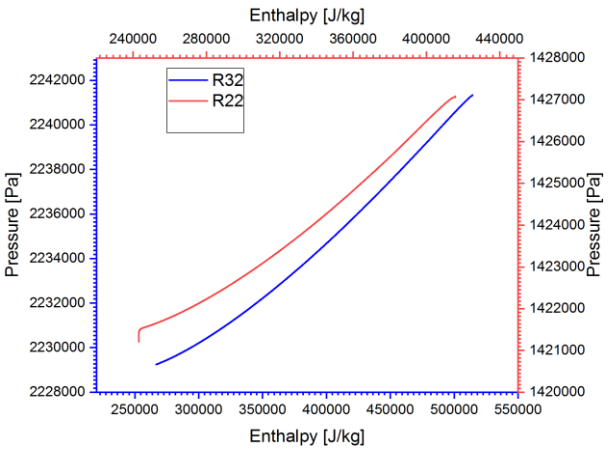

Figure 6. Pressure as a function of enthalpy.

For refrigerants R22 and R32, Figure 7 illustrates how the Reynolds number Re(z) varies throughout the condenser tube when the mass flow rate and shape remain constant. Re steadily declines with axial distance as condensation thickens the liquid layer, lowers the cross-sectional average velocity at constant mass flux, and increases the mixture viscosity μ(z). Re=Gd/μ(z) is consistent with this situation. Re decreases from about 8.30×10^4 at the inlet to approximately 4.42×10^4 across 0–5 m, approximately 1.15×10^4 at z = 10 ± 1 m, approximately 7.74×10^3 at

z= 20 ± 1 m, and approximately 7.51×10^3 over the final 10% of the length. From around 1.03×10^5 at the inlet to roughly 7.96×10^4 across 0–5 m, 2.60×10^4 at z=10±1m, 1.44×10^4 at z=20±1m, and roughly 8.92×10^3 in the last 10%, the trend for R32 is the same throughout a distance of roughly 50 m. These trajectories indicate that the inlet conditions are getting more turbulent and approaching the transitional regime as the mixture temperature decreases near saturation and the liquid percentage increases. Geometrically, *Re* would increase by the same amount for larger tube diameter d and higher mass flux G. According to the existing assumptions, wall roughness mostly impacts pressure losses and the friction factor rather than Re itself.

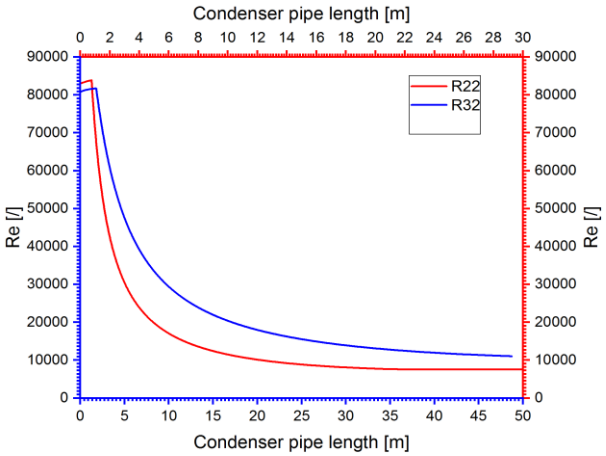

Figure 7. Reynolds number as a function of pipe length.

Table 3 shows the correlations used to generate each of the figures (8-21). The table highlights the changes in the temperature, pressure, density, and velocity of the R22 and R32 refrigerants along the condenser tube.

Table 3: Constants correlations considered for data graphing.

Correlations of	Figures. 8-12	Figures. 13, 15, 17, 19	Figures. 14, 16, 18, 20, 21
α_{sp}	Dittus-Boelter	Dittus-Boelter	Dittus-Boelter
ΔP_{sp}	**variables**	Moody	Moody
α_{tp}	Shah	Shah	Traviss
ΔP_{tp}	Müller-Steinhagen and Heck	**variables**	**variables**

The refrigerant pressure varies along the tube using the three single-phase heat-transfer correlations, as shown in Figure 8. Both refrigerants exhibit a steady decline in the axial pressure distribution along the condenser, indicating that friction dominates the flow in the interior channels. The overall pressure drop for R22 with a 30 m condenser is ΔP ≈ 6.16 kPa, and the average gradient is approximately 205 Pa/m. The inlet and outlet pressures are approximately P_{in} = 1427 kPa and P_{out} ≈ 1421 kPa. The input and output pressures for an R32 with a 50 m condenser are 2242 kPa and 2229kPa, respectively. This procedure leads to an average gradient of roughly 255 Pa m^{-1} and ΔP≈12.8kPa, which is almost 24% more than R22. When compared to the Yao correlation, the Bejan-based pressure profiles have the same numerical values (AARE = 0%, RMSE = 0 Pa). With RMSE ≈ 2.4×10^{-4} Pa and AARE= 4.0×10^{9}% for R22 and RMSE ≈ 0.088 Pa and AARE≈ 4.0×10^{6}% for R32, the Moody's correlation, however, only reveals minor variations. The absolute pressure level (~10 Pa) and the overall pressure drops (kPa range) are much larger than these variances. This finding suggests that the single-phase heat-transfer correlation in this situation does not significantly affect the axial pressure distribution. R32's lower density is mostly responsible for its greater pressure gradient. Higher flow velocities will result from the same mass flow rate, and the frictional term ($\xi\rho u^2/2d$) along the tube will increase due to the viscosity variations. From an engineering standpoint, the most significant factors influencing the pressure-length behavior are the length of the condenser and the characteristics of the refrigerant. When sizing the compressor and condenser, the increased pressure loss of R32 must be considered. The selection of the tested single-phase correlations does not significantly affect the expected axial pressure decrease. Hydrodynamic behavior is not as significant as thermal performance.

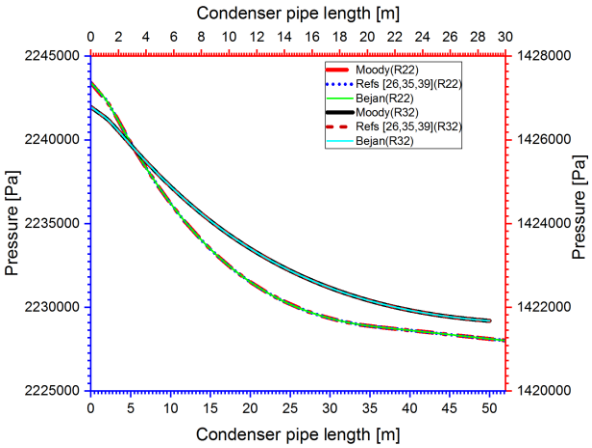

Figure 8. Pressure as a function of pipe length for different correlations used to calculate the heat transfer coefficient in the single-phase region.

For two refrigerants (R22 and R32), Figure 9 shows the evolution of mixture density ρ(z) during condensation using three different single-phase heat-transfer-coefficient frameworks (Refs. [26, 35, 39], Bejan, and Moody). At z = 0 m, ρ increases from

59.99kgm^{-3} to 88.55 kg m^{-3} at 5 m and 153.95 kg m^{-3} at 10 m. Thereafter, it enters the saturated-liquid phase, reaching 1011.08 kg m^{-3} at 20 m and stabilizing at about 1150.57 kg m^{-3} by 30 m. The cross-model standard deviation, interquartile range (IQR), and coefficient of variation (CV) are all 0 on the common grid since the R22 values at each axial station in the three HTC frameworks are identical. This invariance suggests that the saturation envelope and vapor-quality decay, rather than the particular single-phase HTC formula, control the density trajectory under the current operating conditions. For R32, the same monotonic trend is observed—62.33 kg m^{-3} at the inlet, 72.60 kg m^{-3} at 5 m, 87.58 kg m^{-3} at 10 m, 133.69kg/m^3 at 20 m, 426.71 kg m^{-3} at 40 m, and 916.59 kg m^{-3} at 50 m—with dispersion across HTCs that remains negligible: at z ≈ 5 m the range is 72.59656–72.59657 kg m^{-3} with σ ≈ 7.8×10^{-6} kg m^{-3}, CV ≈ 1.07×10^{-5}%, and IQR ≈ 8.3×10^{-6} kg m^{-3}; at z ≈ 40 m the range is 426.706–426.709 kg m^{-3} with σ ≈ 1.25×10^{-3} kg/m^3, CV≈ 2.94×10^{-4}%, and IQR ≈ 1.33×10^{-3} kg m^{-3}; by z≈50 m the spread is effectively vanishing Through U(z) and the local heat flux $\dot{q} \approx U\Delta T$, which determine the condensation rate and, thus, the quality gradient dx/dz, the single-phase HTC correlations physically only indirectly affect ρ(z). Slip decreases, and the mixture density gets closer to the saturated-liquid value as the condensate film thickens downstream; in this regime, phase change and film conduction dominate the total resistance, rendering ρ(z) only slightly sensitive to moderate changes in the selected single-phase HTC.

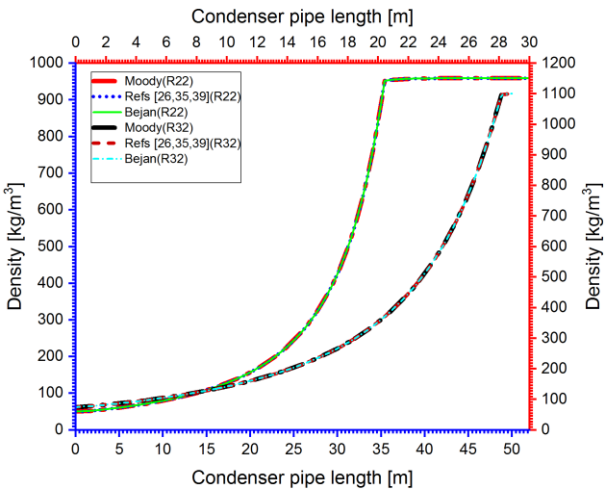

Figure 9. Density as a function of pipe length for different correlations used to calculate the heat transfer coefficient in the single-phase region.

The selection between Refs. [26, 35, 39], Bejan, and Moody has no practical impact on the thermodynamically controlled density evolution under the current fixed configuration, but geometric or operational changes that significantly alter shear and film thickness—smaller diameter, higher mass flux, or increased wall roughness—would raise U and accelerate condensation, potentially amplifying inter-correlation differences.

Figure 10 uses the EVAP COND Reference and three single-phase correlations to show the refrigerant temperature variation along the tube. For R22, the single-phase correlations (Bejan, Yao, and Moody) estimate a total refrigerant temperature loss of roughly 5.0°C across 0–30 m, while the EVAP-COND reference model predicts a temperature drop of roughly 4.0°C. Here are some examples of anchor points: 40.0°C for both at z=0 m; around 37.014°C (correlations) versus 36.9°C (reference) at z=5 m; roughly 36.933°C versus 36.7°C at z=15 m; and roughly 35.0°C versus 36.0°C at z=30 m. Mean absolute error (MAE) = 0.292°C, root mean square error (RMSE) = 0.338°C, bias = -0.267°C (slight overcooling), maximum absolute error (MaxAE)=1.000°C, and normalized RMSE (nRMSE)≈ 0.338 are the agreement metrics of the correlations over the entire duration with respect to EVAP COND. Locally, the metrics are ≈ 0.156/0.170/+0.114/0.114/0.170 over 0–5 m, ≈ 0.320/0.329/+0.233/0.333/0.329 over 15 ± 1 m, and ≈ 0.733/0.800/-0.733/1.000/2.223 over the final 10% of the length. The three correlations for R32 almost collapse onto a single curve over the available span (median dispersion ≈ 0.000°C), with intermediate values of ≈ 35.899°C at z = 5 m and ≈ 35.764°C at z≈25 m and a total drop of ≈ 4.843°C from 40.000°C at z = 0 m to 35.157°C at z ≈ 50 m.

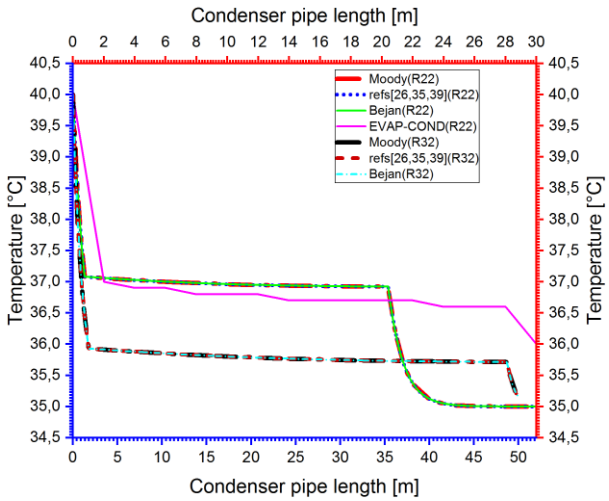

Figure 10. Temperature as a function of pipe length for different correlations used to calculate the heat transfer coefficient in the single-phase region.

The models function hydrodynamically by using the single-phase heat transfer coefficient α, which enters the energy balance as $dT/dz \propto \alpha A/(\dot{M} c_p)$; as a result, roughness and wall condition regulate near-wall

convection, while larger mass flux G and smaller tube diameter d increase α and steepen |dT/dz|. While the mid-length agreement suggests operation in a regime dominated by geometry and operating conditions where differences among Bejan/Refs. [26, 35, 39]/Moody are of second order, the slight overcooling for R22 near the outlet is consistent with a regime where the correlations maintain a relatively high α while the heat capacity flow $\dot{M}\, c_p$ decreases.

Figure 11 shows how the mixing velocity u(z) changes along the length of a tubular condenser for refrigerants R22 and R32. It uses the single-phase heat-transfer-coefficient correlations from Bejan, Refs. [26, 35, 39], and Moody. For R22, u decreases gradually from 2.303m.s^{-1} at z = 0 m to 1.560 m s^{-1} at z = 5 m, 0.897m.s^{-1} at z = 10 m, 0.137 m s^{-1} at z = 20 m, and 0.120 m s^{-1} at z = 30 m. This is a net decrease of roughly 94.79% over the available duration. 2.217m.s^{-1} at the inlet, 1.903 m s^{-1} at 5 m, 1.578 m s^{-1} at 10 m, 1.033 m s^{-1} at 20 m, 0.324 m s^{-1} at 40 m, and 0.151 m s^{-1} at 50 m reveal the same monotonic behavior for R32. This figure represents an overall decline of almost 93.20%. At every location on the shared axial grid, the two correlations show the identical velocities for both fluids. According to this conclusion, there is extremely little inter-model dispersion (σ = 0 m s^{-1}, IQR ≈ 0 m s^{-1}, CV ≈ 0%). From continuity, u = G/(ρA), the hydrodynamic mechanism is directly inferred: as condensation increases, ρ rises while the void fraction and slip decrease, pushing u downward into the saturated-liquid regime.

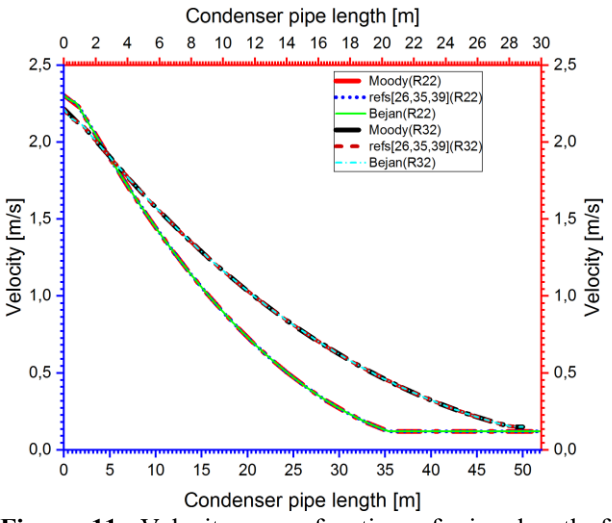

Figure 11. Velocity as a function of pipe length for different correlations used to calculate the heat transfer coefficient in the single-phase region.

The single-phase heat-transfer correlations only affect the local heat flow and the temperature differential between the fluid and the wall. In this instance, ρ(z) and u(z) remain constant across correlations because the influence does not alter the saturation state at the sampled stations. From a geometric point of view, the decay would occur later and the entrance velocity would be higher with a smaller diameter or a bigger mass flux, G. The choice of h may become more sensitive if this variation is coupled with increased frictional losses that alter the saturation trajectory. The principal determinants of velocity change in the current configuration are thermodynamic restrictions, and u(z) is not significantly affected by variations in the heat-transfer correlations used.

Because wall friction is the primary source of loss in Figure 12 (single-phase hot-vapor zone, prior to condensation), the pressure decreases nearly linearly with axial distance. For R32, the ΔP values are 394.2kPa with Moody and 772.3 kPa with Bejan/Refs [26, 35, 39]. The single-phase segment is approximately 1.8 m long (from ~0.737 to 0.343 MPa). This indicates that a drop that is roughly 95.9% bigger is predicted by Bejan/Refs [26, 35, 39]. Each has an average gradient of roughly 429.1 kPa/m and 219.0 kPa/m. R22 has a shorter hot-vapor length of approximately 0.76 m, but its per-meter loss is steeper: ΔP = 381.5 kPa (Moody) compared to 754.1 kPa (Bejan/ Refs. [26, 35, 39]). Accordingly, the average dP/dz increases from 501.9 to 992.3 kPa/m, and Bejan/Refs. [26, 35, 39] is approximately 97.7% higher. In this region, the mean absolute percent deviation is roughly 26.0% for R32 and 26.3% for R22; the difference in ΔP is roughly 58.5% for R32 and 59.2% for R22. The way each correlation maps the friction factor ξ(Re,ε/d) in turbulent vapor is the source of these variations in hydrodynamics: For the same mass flux and diameter, Bejan/Refs. [26, 35, 39] provides a somewhat bigger ξ.

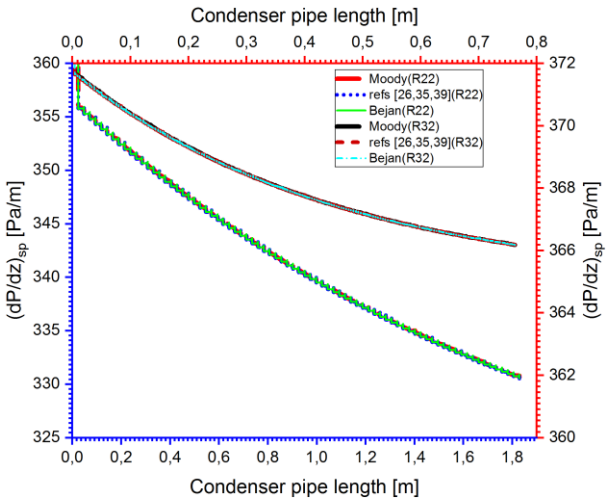

Figure 12. Pressure drops as a function of pipe length for different correlations used to calculate the heat transfer coefficient in the single-phase region.

The Darcy–Weisbach relation causes a higher dP/dz as a direct result. Due to its shorter superheated length and property set at the inlet, the R22 gradient is steeper. Nonetheless, both refrigerants exhibit the anticipated near-linear decline characteristic of friction-dominated, single-phase flow.

In Figure 13, we identify the two-phase pressure drop using four correlations (Müller-Steinhagen and Heck, Friedel, Lockhart-Martinelli, and Chisholm) and the two-phase heat-transfer coefficient using the Shah model. At the inlet (single-phase superheated portion), the pressure decreases approximately linearly before increasing when the flow approaches two-phase. The overall pressure loss (ΔP) for the R32 example over approximately 50 meters is around 8–10 kPa with MSH, 12–18 kPa with Friedel and L–M, and 24–30kPa with Chisholm, according to the shown curves. Consequently, the sequence of ΔP from smallest to largest remains unchanged: MSH < Friedel ≈ L–M < Chisholm. Depending on where you are along the tube, the mean absolute deviation (MAD) is roughly 25–30% around the average, and the dispersion index is roughly 80–120%. On a shorter length scale, the same pattern is true for R22 over a distance of roughly 30 m: ΔP is roughly 6–8 kPa for MSH, 9–13 kPa for Friedel/L–M, and 15–18 kPa for Chisholm. The mean absolute deviation is roughly 20–25%, and the relative scatter is roughly 60–80%. From an engineering perspective, the most crucial factor in determining the power requirements of the compressor and fan is the selection of the two-phase pressure-drop correlation: Friedel or L-M is a suitable middle ground; Chisholm has the most pumping demand, while MSH has the lowest. Before the curves level off as a thicker liquid layer forms and x moves downstream, the two-phase shear resistance rises with vapor quality x (increased wall and interfacial shear), making dP/dz steeper.

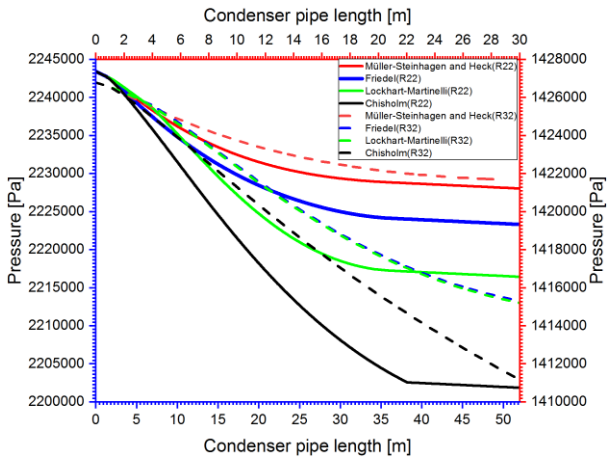

Figure 13. Pressure as a function of pipe length using different correlations for two-phase pressure drops, based on the Shah model for the two-phase heat transfer coefficient.

Figure 14 retains the four pressure-drop correlations but substitutes the Traviss model for the Shah model for the two-phase heat-transfer coefficient. Because h regulates the rate of enthalpy removal and, consequently, the axial distribution of vapor quality x(z), the form of the pressure–length trajectories changes while the order of ΔP among the correlations remains constant. The reduction in z is delayed, and the frictional gradient lasts longer (a steeper drop that lasts longer downstream) if Travis anticipates a lower α in the current flow regime. Conversely, the pressure-drop curve flattens out sooner, density increases sooner, and z drops quicker if Traviss forecasts a greater α. While the absolute size of ΔP is still largely controlled by the frictional correlations, the difference between Shah and Traviss dictates where and when latent heat is extracted (the condensation rate and the change in enthalpy). To achieve the intended hydraulic margin, first set up the two-phase pressure-drop model for design (MSH for a lower bound, Chisholm for an upper bound, and Friedel/L–M as balanced choices). In order to achieve both thermal performance (completion of condensation over a shorter length) and hydraulic cost (lower dP/dz and ΔP), the thermal duty is then divided along the condenser using heat-transfer sensitivity (Shah versus Traviss) by selecting d, ε/d, and mass flux G.

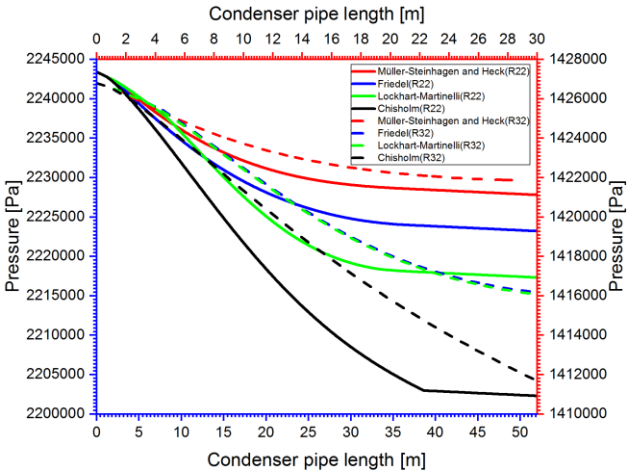

Figure 14. Pressure as a function of pipe length using different correlations for two-phase pressure drops, based on the Traviss model for the two-phase heat transfer coefficient.

Using four canonical two-phase pressure drop correlations (MSH, Friedel, Lockhart–Martinelli, and Chisholm) and the Shah model for the two-phase heat transfer coefficient, Figure 15 demonstrates that condenser density profiles for R32 show a noticeable correlation-dependent dispersion, rather than the near collapse seen for R22. With MSH forecasting 0.500, the R32 outlet density from the exported datasets ranges from 0.100 (Chisholm) to 0.595–0.591 (L–

M/Friedel); the mean is 0.447. With a mean absolute deviation (MAD) of about 38.8% and a dispersion index ($(\rho_{max}-\rho_{min})/\rho_m$) of around 110.9%, this procedure shows that the exit state is highly sensitive to the frictional model. For MSH/Friedel, the average gradients are O(0.00010–0.00010) per length unit (same for L–M), whereas Chisholm is smaller on average (0.00001), which is consistent with a longer vapor-rich stretch prior to ρ(z) flattening. With dispersion ≈0.0% and MAD ≈0.0%, the four correlations for R22 converge to about the same outlet density (0.300 ≈ 0.300 ≈ 0.300 ≈ 0.300). MSH and the mid-range Friedel/L-M imply lower frictional penalties and earlier liquid film thickening, hence higher ρ_{out}. Hydrodynamically, the higher two-phase interfacial and wall shear embedded in Chisholm sustains a larger vapor quality over distance, depressing the mixture density at the exit.

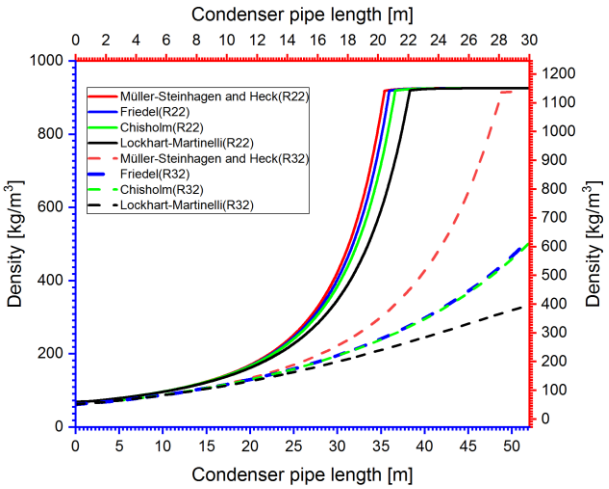

Figure 15. Density as a function of pipe length using different correlations for two-phase pressure drops, based on the Shah model for the two-phase heat transfer coefficient.

The ranking (MSH < Friedel ≈ L–M < Chisholm) remains unchanged when the Traviss model is substituted for Shah in Figure 16 for the two-phase heat transfer coefficient while keeping the same four pressure drop correlations. However, the axial density evolution is reshaped by the enthalpy removal rate. A lower h prediction postpones this transition, keeping the mixture lighter for longer; a higher h forecast speeds up condensation, increases density quicker, and causes an earlier flattening of ρ(z). Thermodynamically, the trajectory x(z), or the location and speed at which latent heat is extracted, is determined by the Shah–Traviss replacement, but the frictional model still largely controls the amount of outlet density dispersion. In order to balance thermal performance (shorter length/higher ρ_{out}) with hydrodynamic constraints (acceptable dP/dz and overall ΔP) for both R32 and R22, one should first perform a heat transfer sensitivity (Shah vs. Traviss) to allocate the thermal duty along the condenser (choosing d, ε/d, and mass flux G). This is done by first bounding the hydraulic cost by choosing the ΔP correlation to meet compressor/fan margins (MSH for a lower bound, Chisholm for an upper bound, and Friedel/L–M as balanced choices).

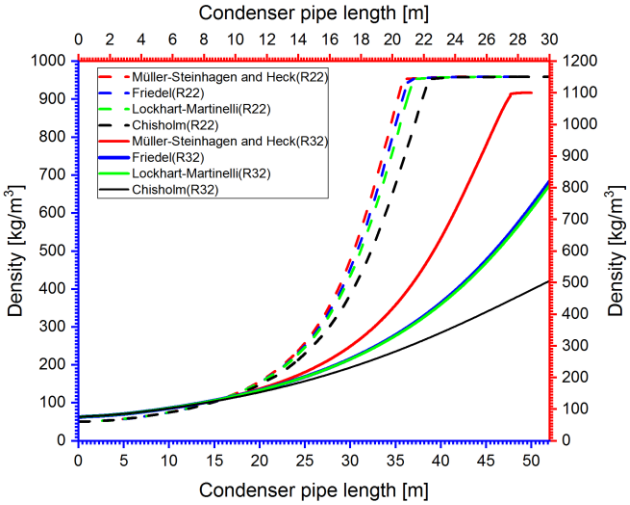

Figure 16. Density as a function of pipe length using different correlations for two-phase pressure drops, based on the Traviss model for the two-phase heat transfer coefficient.

Figure 17 displays the axial temperature profiles T(z) for R22 and R32 that we determined using the Shah boiling heat-transfer correlation. The frictional pressure loss was calculated using the following four conventional correlations: Chisholm, Lockhart–Martinelli, Müller–Steinhagen and Heck, and Friedel. At the R22 intake, all four profiles cool from 40.0°C to approximately 35.00°C at the outflow (ΔT=5.00°C). For every unit of z, the best-fit slopes are -0.088, −0.086, -0.089, and -0.081°C. When compared to the Evap-Cond reference (R22), the variations are still negligible: Friedel (MAE 0.606°C, RMSE 0.961°C), Chisholm (MAE 0.538°C, RMSE 0.891°C, max |ΔT| 1.800°C, bias -0.515°C), Lockhart–Martinelli (MAE 0.567°C, RMSE 0.940°C), and MSH (MAE 0.641°C, RMSE 0.978°C). Predictions are a bit colder near the end of the tube because the mean bias is slightly negative (around -0.511°C) and the largest pointwise deviation is approximately 1.800°C. For R32, the same three-stage pattern occurs, but ΔT varies between 4.60 and 5.21°C across correlations (minimum temperatures between 35.396 and 34.790°C). It is hence more sensitive in the vicinity of dryout.

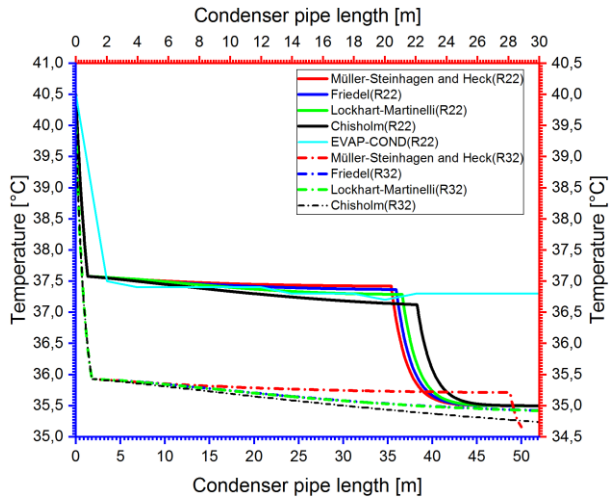

Figure 17. Temperature as a function of pipe length using different correlations for two-phase pressure drops, based on the Shah model for the two-phase heat transfer coefficient.

Figure 18 illustrates the pressure loss variation of the refrigerant along the condenser tube in the two-phase region, calculated based on four commonly used relationships: Friedel, Chisholm, Lockhart and Martinelli (LM), and Müller-Steinhagen and Heck (MSH). It is evident that the pressure losses are not uniform along the condenser: they increase rapidly at the beginning of the two-phase region, reach a maximum, and then gradually decrease toward the tube outlet. This behavior reflects the gradual transition of flow regimes as the refrigerant condenses. Significant quantitative differences are observed between the models.

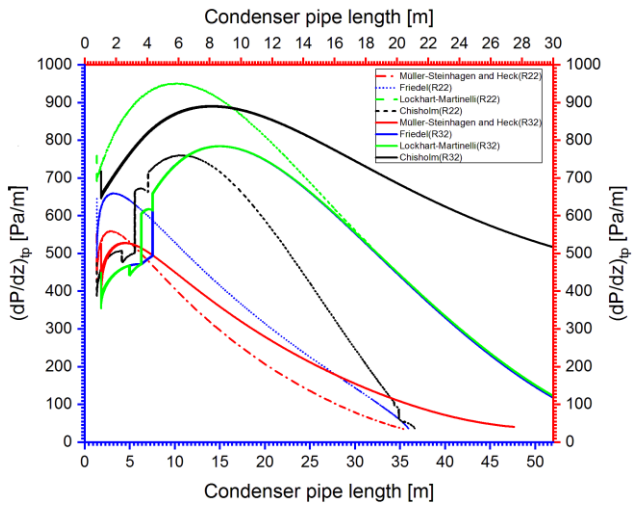

Figure 18. Pressure drops as a function of pipe length using different correlations for two-phase pressure drops, based on the Traviss model for the two-phase heat transfer coefficient.

The MSH relationship predicts the highest values, with a maximum of approximately 0.55 kPa/m², while the Friedel, Chisholm, and LM values reach approximately 0.65 kPa/m², 0.75 kPa/m², and 0.95 kPa/m², respectively, for R22. These discrepancies represent an overestimation of 25% to 70% compared to the other relationships. The maximum location is approximately 2 meters for the MSH and Friedel models. And 6 meters for the remaining correlations. At the end of the condenser, the LM predicts approximately 0.40 kPa/m³, while pressure drops tend to be negligible. For the other correlations, R32 exhibits similar behavior, with variations in values primarily attributed to differences in the dynamic viscosity and density of each refrigerant.

The axial condenser pressure profile P(z) for refrigerants R22 and R32, calculated using the Travis boiling heat-transfer correlation, is shown in Figure 19. Four models (Friedel, Lockhart–Martinelli, Müller–Steinhagen & Heck, and Chisholm) are used to determine the frictional pressure drop. Friedel forecasts the highest decline for R22 over z≈0.77–22 m (ΔP = 478.65 kPa (ΔP% = -92.82%, $dP/dz = -32.88 \text{kPa per unit z}$)), followed by MSH (409.66kPa, -92.03%, -29.18) and Chisholm (365.23kPa, -91.10%, -29.45); Lockhart–Martinelli predicts a smaller reduction (334.43kPa, -47.61%, −25.85). MSH is slightly bigger (360.91 kPa, −89.91%, -11.94) for R32 across a longer span (z=1.81–50 m), while Chisholm yields a weaker drop (252.07 kPa, -38.38%, -5.63). Friedel and Lockhart–Martinelli cluster near ΔP ≈ 331.4 kPa (ΔP ≈ -89%, dP/dz ≈ -12.4). P(z) always declines monotonically, with the largest variations appearing in the outlet portion.

In terms of hydrodynamics, the pressure loss is made up of a lower accelerational component and a larger frictional component (the gravitational term is insignificant for a horizontal condenser). Higher slip ratios and high vapor quality near the intake increase interfacial shear; correlations that increase two-phase friction (Friedel, MSH) hence predict larger ΔP and steeper dP/dz. The liquid film thickens, the accelerational contribution decreases, the void percentage and vapor quality decrease, and dP/dz flattens as condensation continues. The relatively low ΔP from Chisholm in R32 and Lockhart-Martinelli in R22 suggests slip or void-fraction assumptions that lower effective interfacial shear along the length. With the greatest sensitivity in the terminal region, where slight variations in two-phase friction significantly alter p_{sat} (z) and the necessary condensation driving temperature, these trends suggest that, geometrically, for fixed diameter and roughness, the condenser (tube count and length) and compressor/pump head should be sized to treat Friedel/MSH as upper-bound pressure-loss designs and Chisholm as a lower bound.

Figures 19 and 20 illustrate the variation in refrigerant velocity based on the length of the condenser tube, calculated using four correlations: Friedel, Chisholm, LM, and MSH. Note that the refrigerant velocity gradually decreases along the condenser tube. This decrease is due to the gradual condensation of the refrigerant gas into a liquid, resulting in a reduction in flow velocity. The four correlations contain nearly identical sets, demonstrating the limited impact of these correlations on the accuracy of predicting condenser behavior.

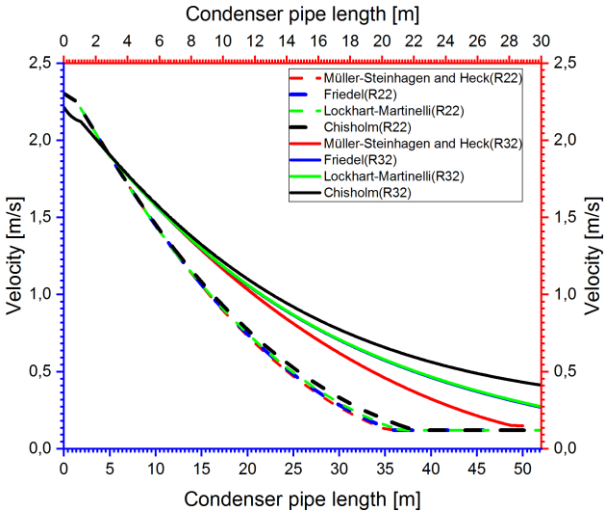

Figure 19. Velocity as a function of pipe length using different correlations for two-phase pressure drops, based on the Shah model for the two-phase heat transfer coefficient.

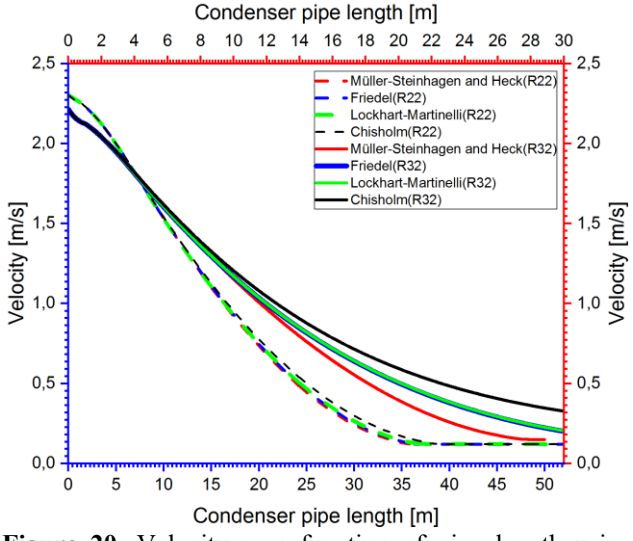

Figure 20. Velocity as a function of pipe length using different correlations for two-phase pressure drops, based on the Traviss model for the two-phase heat transfer coefficient.

The same four pressure-drop models are displayed once more in Figure 21, but this time the Traviss boiling heat-transfer correlation is used. For both refrigerants, the axial temperature decline maintains its three-stage form. With fitted slopes of -0.088, -0.086, -0.089, and -0.081°C per unit z, ΔT for R22 remains at roughly 5.00°C. With slopes of -0.013, -0.013, -0.012, and −0.013°C per unit z, the end-to-end dips for R32 are 4.604, 4.611, 4.843, and 5.210°C. According to Chisholm, MSH has a somewhat higher exit temperature, whereas R32 cools the most across correlations ($\Delta T = 5.210°C$, $T_{min} \approx 34.790°C$). The local saturation temperature is primarily affected by frictional pressure-drop models toward the tube's end, where the discrepancies are most apparent.

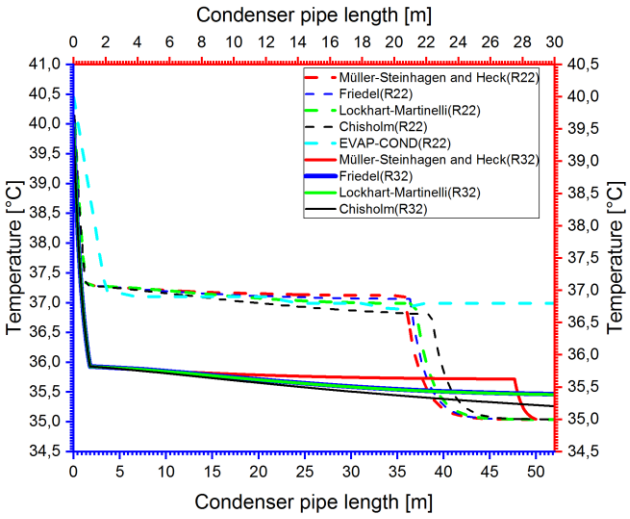

Figure 21. Temperature as a function of pipe length using different correlations for two-phase pressure drops, based on the Traviss model for the two-phase heat transfer coefficient.

8. VALIDATION MODEL

The current model (R32 in a copper tube at 37°C) was validated by comparing it with experimental results reported in the paper "Condensation heat transfer of R22, R410A, and R32 inside a multiport mini-channel tube" [40] (See Figure 22). The experimental data in the reference study showed similar trends to the current model regarding the effect of mass flow and added heat on the heat transfer coefficient. The input data from the experimental study were inadequate for attaining enhanced concordance; however, the overarching trends between the two models remained consistent. However, the study recommends the use of micro-port tubes, which demonstrated superior heat transfer performance compared to copper tubes. Therefore, the current model can be validated based on experimental agreement and comparisons of mass flow and added heat, while acknowledging the need to improve performance by increasing mass flow or using more sophisticated designs such as micro-port tubes. To ensure the validity of the current model, axial temperature profiles T(z) for R22 were compared against the Evap-Cond reference over the span $z \in [0, 30\ m]$. Model curves were resampled onto

the reference grid, and pointwise errors were computed. The summary metrics obtained—$RMSE = 0.86\,°C$, $MAE = 0.86\,°C$, $max\,|\varepsilon| = 1.78\,°C$, and $Bias = -0.395\,°C$—showed a small negative bias, indicating slightly cooler predictions near the outlet. Measurement accuracy was incorporated using an uncertainty-aware acceptance rule, which was satisfied under realistic instrumentation conditions, with $U \approx \pm 1.0\,°C$ (expanded, $k = 2$). While the Pearson correlation ($r = 0.553$) was reported, it was not used as a rigorous criterion due to the monotonic nature and limited dynamic range of both profiles. This data supports the validation of the current model based on the overall agreement with experimental trends, although improvements could be made, as suggested by the experimental findings and the recommendation for using advanced micro-port tube designs.

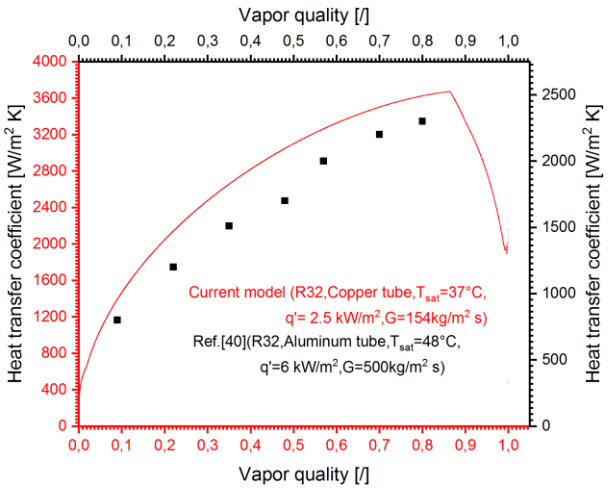

Figure 22. Comparison of Heat Transfer Coefficients Between the Current Model and Experimental Results from Reference [40] Under Different Operating Conditions.

9. CONCLUSIONS

This work developed a steady-state numerical model of a condenser and analyzed the effects of refrigerant properties and pressure-drop correlations on coupled thermal–hydraulic behavior. The long-standing assumption of refrigerant compressibility along the condenser is not supported: in the third region the refrigerant behaves effectively incompressibly, which simplifies the local mass and momentum balances and limits the propagation of pressure-related effects to other fields. Seven pressure-drop correlations were assessed, four of which target the two-phase zone; employing the more accurate formulations yielded clear improvements in numerical performance and closer agreement with the reference solution.

Building on these results, the choice of pressure-drop correlation primarily affects the axial gradient, total pressure loss, and pumping requirements, whereas the principal physical and thermodynamic fields remain nearly invariant: axial temperature distributions, two-phase length, and vapor-quality trajectories change only marginally. Relative to EVAP-COND, the model achieved very high thermal accuracy for both refrigerants and for both heat-transfer-coefficient options, with mean absolute error and root-mean-square error below $0.4\,°C$, mean absolute percentage error below 1%, and coefficients of determination exceeding 0.998. For pressure drop, sensitivity to the correlation is higher: Müller–Steinhagen and Heck and Friedel show the lowest overall deviation ($\approx 4-6\%$), Chisholm exhibits a positive bias ($\approx 5-12\%$), and Lockhart–Martinelli a negative bias ($\approx 5-10\%$), with the performance ranking essentially unchanged along the condenser. Practically, these findings enable designers to select condenser geometries that achieve complete condensation with minimal pressure loss while maintaining thermal stability; the most effective control levers are geometric—adjusting inner diameter, the number of parallel circuits, adopting micro-fin tubes, and enhancing the air side—whereas the correlation choice chiefly influences pumping estimates and allowable pressure-drop margins rather than the qualitative structure of the thermal fields.

Conducting experimental research under various conditions, such as partial load operation and minimal dehumidification in dry-wet cooling mode, can yield additional insights. Researchers should also develop models that account for variations in refrigerants used in commercial systems.

Advancements in numerical modeling technology and methodology such as lower costs, more sophisticated software and larger datasets across industries and research facilities will further improve simulation accuracy. In future two-scale designs, the core-scale heat exchanger and its modules (condenser and two-phase heat exchanger) can be solved simultaneously.

Enhancing the entire numerical model will require developing more reliable friction correlations and a fully integrated two-scale model. These advancements will contribute to the continued optimization of cooling systems, ultimately leading to more efficient condensers and improved full-scale refrigeration systems.

APPENDIX A: SPECIAL PARAMETERS OF THE GOVERNING EQUATIONS IN THE Two-PHASE REGION

Mixture density [31, 41]

$$\rho_{tp} = \psi\rho_g + \rho_l(1-\psi) \tag{54}$$

For homogeneous flow [32, 41]

$$u = u_g = u_l = G\rho_{tp}^{-1} \tag{55}$$

Where [42, 43]

$$\psi = \left[1 + \left(\rho_g - x\rho_g\right)/(x\rho_l)\right]^{-1} \quad (56)$$

Mixture total enthalpy [27, 31]

$$h_{tp} = xh_g + h_l(1-x) \quad (57)$$

The term B is presented in (eq.24) as follows [32, 35]:

$$B = x^2\left[1 + \frac{\rho_l(1-\psi)}{\psi\rho_g}\right] + (1-x)^2\left[1 + \frac{\psi\rho_g}{\rho_l(1-\psi)}\right] \quad (58)$$

APPENDIX B: PRESSURE DROPS

- For a single-phase region [44, 45]:

$$\Delta P_{sp} = \frac{\rho_{sp}u^2\xi_D}{2d}\Delta z_i = F_{f,sp}\,\Delta z_i \quad (59)$$

Based on Bejan [27], the Darcy friction factor is calculated:

$$\xi_D = \begin{cases} \frac{64}{Re} & Re < 2000 \\ \frac{0.078}{Re^{0.25}} & 2000 \le Re \le 8\times10^4 \\ \frac{0.046}{Re^{0.3}} & Re > 8\times10^4 \end{cases} \quad (60)$$

Based on Hagen-Poiseuille, Blasius, and Hermann correlations [26, 35, 39], the Darcy friction factor is calculated:

$$\xi_D = \begin{cases} \frac{64}{Re} & Re < 2320 \\ \frac{0.3164}{Re^{0.25}} & 2320 \le Re \le 8E4 \\ 0.0054 + \frac{0.3964}{Re^{0.3}} & Re > 8E4 \end{cases} \quad (61)$$

Based on Moody [46], the Darcy friction factor is calculated (see figure 23):

$$\xi_D = 0.0055\left[1 + \left(\frac{10^6}{Re} + 20000\frac{e}{d}\right)^{0.33}\right] \quad (62)$$

For pipe of Carbon steel, commercial, the relative roughness of pipe $e = 0.045\,mm$ [46], for more information, see the reference [46].

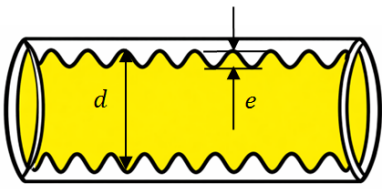

Figure 23. Relative roughness of pipe [47].

Dittus-Boelter equation [35, 48]

$$\alpha_{sp} = 0.023d^{-1}Re^{0.8}Pr^{0.4}\lambda \quad (63)$$

Where [32, 37, 49]

$$Re = \rho_{sp}ud\mu^{-1} \quad (64)$$

And [49]

$$Pr = \mu c_p\lambda^{-1} \quad (65)$$

- For a two-phase region:

Müller-Steinhagen and Heck correlation [35, 44, 50]

$$\Delta P_{tp} = \left[\Delta P_{lo} + 2\left(\Delta P_{go} - \Delta P_{lo}\right)x\right](1-x)^{0.33} + \Delta P_{go}\,x^3 = F_{f,tp}\,\Delta z_i \quad (66)$$

Friedel correlation [14, 44, 50]

$$\Delta P_{tp} = \Delta P_{lo}\left(\frac{3{,}24C_2C_3}{We_l^{0.035}Fr^{0.045}} + C_1\right)^2 = F_{f,tp}\,\Delta z_i \quad (67)$$

Where

$$C_1 = x^2\left(\frac{\rho_l\Delta P_g}{\rho_g\Delta P_l}\right)(1-x)^2 \quad (68)$$

$$C_2 = x^{0.78}(1-x)^{0.224} \quad (69)$$

$$C_3 = \left(\frac{\rho_l}{\rho_g}\right)^{0.91}\left(\frac{\mu_g}{\mu_l}\right)^{0.19}\left(1 - \frac{\mu_g}{\mu_l}\right)^{0.7} \quad (70)$$

Froude number [14, 44, 51]

$$Fr = \frac{G^2}{gd\rho_{tp}^2} \quad (71)$$

Weber number [14, 44, 51]

$$We_l = \frac{G^2d}{\sigma\rho_{tp}} \quad (72)$$

Lockhart and Martinelli correlation [15, 44, 51]

$$\Delta P_{tp} = F_{f,tp}\,\Delta z_i = \begin{cases} C_4\Delta P_l & Re_{lo} > 4000 \\ C_5\Delta P_g & Re_{lo} < 4000 \end{cases} \quad (73)$$

Where

$$C_4 = 1 + \frac{C_6}{X_{tt}} + \frac{1}{X_{tt}^2} \quad (74)$$

$$C_5 = 1 + C_6X_{tt} + X_{tt}^2 \quad (75)$$

$$C_6 = \begin{cases} 20 & Re_{lo} > 2000\ and\ Re_{go} > 2000 \\ 12 & Re_{lo} < 2000\ and\ Re_{go} > 2000 \\ 10 & Re_{lo} > 2000\ and\ Re_{go} < 2000 \\ 5 & Re_{lo} < 2000\ and\ Re_{go} < 2000 \end{cases} \quad (76)$$

Chisholm correlation [15, 51, 52]

$$\Delta P_{tp} = F_{f,tp}\,\Delta z_i = \Delta P_{lo}[1 + (C_7^2 - 1) + C_8x^{0.875}(1-x)^{0.875} + x^{1.75}] \quad (77)$$

Where the dimensionless parameter C_7 is defined by:

$$C_7^2 = \frac{\Delta P_{go}}{\Delta P_{lo}} \quad (78)$$

The coefficient C_8, which accounts for the interaction between the phases, is defined piecewise as a function of C_7 and the mass flux G:

$$C_8 = \begin{cases} 55G^{-0.5} & 0 < C_7 \le 9.5 \ and \ G \ge 1900 \\ 2400G^{-1} & 0 < C_7 \le 9.5 \ and \ 500 < G < 1900 \\ 4.8 & 0 < C_7 \le 9.5 \ and \ G \le 500 \\ 520C_7^{-1}G^{-0.5} & 9.5 < C_7 \le 28 \ and \ G \le 600 \\ 21C_7^{-1} & 9.5 < C_7 \le 28 \ and \ G > 600 \\ 15000C_7^{-2}G^{-0.5} & C_7 > 28 \end{cases} \quad (79)$$

And [18, 39, 51]

$$\frac{\Delta P_l}{\Delta z_i} = \frac{2\xi_{F,lo}G^2(1-x)^2}{\rho_l d} \quad (80)$$

$$\frac{\Delta P_g}{\Delta z_i} = \frac{2\xi_{F,go}G^2x^2}{\rho_g d} \quad (81)$$

$$\frac{\Delta P_{lo}}{\Delta z_i} = \frac{2\xi_{F,l}G^2}{\rho_l d} \quad (82)$$

$$\frac{\Delta P_{go}}{\Delta z_i} = \frac{2\xi_{F,g}G^2}{\rho_g d} \quad (83)$$

Where [39, 44]

$$\xi_{F,l} = \begin{cases} \frac{16}{Re_{lo}} & Re_{lo} < 1187 \\ \frac{0.0791}{Re_{lo}^{0.25}} & Re_{lo} \ge 1187 \end{cases} \quad (84)$$

$$\xi_{F,g} = \begin{cases} \frac{16}{Re_{go}} & Re_{go} < 1187 \\ \frac{0.0791}{Re_{go}^{0.25}} & Re_{go} \ge 1187 \end{cases} \quad (85)$$

Hagen–Poiseuille and McAdams correlation [52-54]

$$\xi_{F,lo} = \begin{cases} \frac{16}{Re_l} & Re_l < 1500 \\ \frac{0.046}{Re_l^{0.2}} & Re_l \ge 1500 \end{cases} \quad (86)$$

$$\xi_{F,go} = \begin{cases} \frac{16}{Re_g} & Re_g < 1500 \\ \frac{0.046}{Re_g^{0.2}} & Re_g \ge 1500 \end{cases} \quad (87)$$

Where

$$Re_{lo} = Gd\mu_l^{-1} \quad (88)$$

$$Re_{go} = Gd\mu_g^{-1} \quad (89)$$

$$Re_l = G\mu_l^{-1}(1-x)d \quad (90)$$

$$Re_g = G\mu_g^{-1}xd \quad (91)$$

$$Re_{tp} = \frac{Gd}{\mu_l}\left[(1-x) + x\sqrt{(\rho_l/\rho_g)}\right] \quad (92)$$

The Lockhart–Martinelli parameter X_{tt} is the ratio of single-phase frictional pressure-drop baselines (liquid-only to gas-only) evaluated at the same mass flux and geometry; for the turbulent–turbulent case [39, 53]:

If $Re_l > 1500 \ and \ Re_g > 1500$, then

$$X_{tt} = (\mu_l/\mu_g)^{0.1}[(1-x)/x]^{0.9}(\rho_g/\rho_l)^{0.5} \quad (93)$$

else

$$X_{tt} = (\xi_{F,lo}/\xi_{F,go})^{0.5}(\rho_g/\rho_l)^{0.5}[(1-x)/x] \quad (94)$$

Traviss correlation [55]

$$\alpha_{tp} = \lambda_l Re_l^{0.9} Pr_l (dC_9)^{-1} \phi(X_{tt}) \quad (95)$$

Where

$$C_9 = \begin{cases} C_{10} & Re_l < 50 \\ C_{11} & 50 < Re_l < 1125 \\ C_{12} & Re_l > 1125 \end{cases} \quad (96)$$

$$C_{10} = 0.707 Re_l^{0.5} Pr_l \quad (97)$$

$$C_{11} = 5Pr_l + 5\ln[1 + Pr_l \ (0.09636Re_l^{0.585} - 1)] \quad (98)$$

$$C_{12} = 5Pr_l + 5\ln(1 + 5Pr_l) + 2.5\ln(0.00313Re_l^{0.812}) \quad (99)$$

$$\phi(X_{tt}) = 0.15|X_{tt}^{-1} + 2.85X_{tt}^{-0.476}| \quad (100)$$

Shah correlation [9, 30]

$$\alpha_{tp} = \frac{0.023\lambda_l Pr_l^{0.4} Re_l^{0.8}}{d(1-x)^{0.8}}\left[(1-x)^{0.8} + \frac{3.8x^{0.76}(1-x)^{0.04}}{P_{red}^{0.38}}\right] \quad (101)$$

Where

$$P_{red} = P_{sat}/P_{crit} \quad (102)$$

Akers et al correlation [51, 54]

$$\alpha_{tp} = \lambda_l C_{13} Re_{tp}^n Pr_l^{0.33} d^{-1} \quad (103)$$

Where

$$C_{13} = \begin{cases} 0.0265, n = 0.8 & Re_{tp} > 5 \times 10^4 \\ 5.03, n = 0.33 & Re_{tp} < 5 \times 10^4 \end{cases} \quad (104)$$

Dobson and Chato correlation [51, 55]

$$\alpha_{tp} = 0.023 Re_l^{0.8} Pr_l^{0.4} \lambda_l (1 + 2.22X_{tt}^{-0.89})/d \quad (105)$$

Chen correlation [15, 21]

$$\alpha_{tp} = 0.023\lambda_l C_{14} Pr_l^{0.4} Re_l^{0.8}/d \quad (106)$$

Where

$$C_{14} = \begin{cases} 1 & X_{tt}^{-1} \le 0.1 \\ 2.35(X_{tt}^{-1} + 0.213)^{0.736} & X_{tt}^{-1} > 0.1 \end{cases} \quad (107)$$

APPENDIX C: Compact Heat Exchanger

Specific heat at pressure constant of pipe wall [13, 26]

$$c_{p,pw} = (c_{p,pipe}M_{pipe} + c_{p,fin}M_{fin})/M_{pw} \quad (108)$$

Superficial efficacy [26, 53]

$$\eta_A = 1 - A_{fin}(1 - \mu_{fin})/A_o \quad (109)$$

$$A_o = N_{line}N_{row}\pi D\left[\left(1-\frac{eN_{fin}}{L_{fin}}\right)+\left(\frac{4\Delta z_j\Delta z_k}{\pi D^2}-1\right)\frac{DN_{fin}}{2L_{fin}}\right] \quad (110)$$

$$A_{fin} = \pi D^2 N_{line}N_{row}\left(\frac{4\Delta z_j\Delta z_k}{\pi D^2}-1\right)\frac{N_{fin}}{2L_{fin}} \quad (111)$$

The fin efficiency for fins with a cylindrical basis is [26, 38]:

$$\eta_{fin} = \frac{tgh\left\{0.5(\Delta z_j - D)\left[1.7\alpha_a/(\lambda_{fin}\varepsilon)\right]^{0.5}\right\}}{0.5(\Delta z_j - D)\left[1.7\alpha_a/(\lambda_{fin}\varepsilon)\right]^{0.5}} \quad (112)$$

Sensible heat transfer coefficient [26]

$$\alpha_a = JG_a c_{p,a}\left(\mu_a c_{p,a}/\lambda_a\right)^{-0.66} \quad (113)$$

Where [26, 38]

$$J = \left[\frac{1-1280N_{row}Re_1^{-0.5}}{1-5120Re_1^{-0.5}}\right]\times[0.0014+0.2618*JP*J(s)] \quad (114)$$

$$JP = Re_2^{-0.4}A_o/A_{to} \quad (115)$$

$$J(s) = 0.84 + 4\times10^{-5}Re_s^{1.25} \quad (116)$$

$$Re_1 = G_a\Delta z_k/\mu_a \quad (117)$$

$$Re_2 = G_a D/\mu_a \quad (118)$$

$$Re_s = G_a s/\mu_a \quad (119)$$

$$G_a = \rho_a u_a \quad (120)$$

$$\dot{M}_a = \rho_a u_a A_{min} \quad (121)$$

$$A_{min} = N_{line}\left(\Delta z_j - D\right)\left(1-\varepsilon N_{fin}/L_{fin}\right) \quad (122)$$

$$A_{to} = N_{row}N_{line}\pi D\left(1-\varepsilon N_{fin}/L_{fin}\right) \quad (123)$$

NOMENCLATURE

A Surface area per unit length of the pipe (m^2/m)
a_z Preismann weighting parameter
c_p Specific heat $(J\ kg^{-1}\ K^{-1})$
D External diameter of pipes (m)
d Internal diameter of pipes (m)
e Relative roughness of pipe (m)
F Force per unit volume $(N\ m^{-3})$
G Mass velocity $(kg\ m^{-2}s^{-1})$
h Enthalpy total $(J\ kg^{-1})$
i, j, k Coordinate
L Length (m)
M Mass (kg)
$\dot{M}$ Mass flow rate $(kg\ s^{-1})$
N Fin number or line number
P Pressure (Pa)
$\dot{q}$ Local heat flux $(W\ m^{-2})$
Pr Prandtl number
Re Reynolds number
s Fin spacing (m)
T Absolute temperature (K)
t Time (s)
U Overall heat transfer coefficient $(W\ K^{-1}\ m^{-2})$
u Velocity (m)
x Vapor quality
X_{tt} Lockhart- Martinelli parameter
z Coordinate (m)

Greek symbols

α Heat transfer coefficient $(W\ K^{-1}\ m^{-2})$
Δ Difference
ΔP Pressure drops (Pa/m)
η Fin efficiency
λ Heat conductivity $(W\ K^{-1}m^{-1})$
μ Dynamic viscosity $(Pa\ s)$
ξ Friction factor
ε Fin thickness (m)
ρ Density $(kg\ m^{-3})$
ψ Void fraction
Γ Mass flow per unit volume $(kg\ s^{-1}\ m^{-3})$

Subscripts

a Air
$Crit$ Critical
D Darcy
F Fanning
f Friction
fI Interfacial fractional factor
fin Fins
H Heat exchanger height
Igl Interface between vapor phase and liquid phase
Ilg Interface between liquid phase and vapor phase
g Gas in mixture
gI The vapor phase at the interface
gl From vapor to liquid
go Gas only
l Liquid in mixture
lI The liquid phase at the interface
$line$ Line of pipes
lg From liquid to vapor
lo Liquid only
m Average value
min Minimal surface area
o Total surface area
$pipe$ Pipes
pw Pipe wall
r Refrigerant
red Reduced
row Row of pipes
sat Saturation or saturation point
sp Single-phase
tp Two-phase

to Pipe surface area without fins

REFERENCES

[1] A. Roccato, M. Uyttendaele, and J.-M. Membré, "Analysis of domestic refrigerator temperatures and home storage time distributions for shelf-life studies and food safety risk assessment," Food Research International, vol. 96, pp. 171-181, 2017. doi: 10.1016/j.foodres.2017.02.017

[2] P. D. Gaspar and P. D. da Silva, "Handbook of research on advances and applications in refrigeration systems and technologies," 2015.

[3] R. Hatchett, "The medicines refrigerator and the importance of the cold chain in the safe storage of medicines," Nursing Standard (2014+), vol. 32, p. 53, 2017. doi: 10.7748/ns.2017.e10960

[4] F. van Holsteijn and R. Kemna, "Minimizing food waste by improving storage conditions in household refrigeration," Resources, Conservation and Recycling, vol. 128, pp. 25-31, 2018. doi: 10.1016/j.resconrec.2017.09.012

[5] K. J. Chua, S. K. Chou, W. Yang, and J. Yan, "Achieving better energy-efficient air conditioning–a review of technologies and strategies," Applied energy, vol. 104, pp. 87-104, 2013. doi: 10.1016/j.apenergy.2012.10.037H.

[6] J.-S. Oh, M. Binns, S. Park, and J.-K. Kim, "Improving the energy efficiency of industrial refrigeration systems," Energy, vol. 112, pp. 826-835, 2016. doi: 10.1016/j.energy.2016.06.119

[7] H. Ramadan and A. Cappenberg, "Uji Prestasi Refrigeran R22 Pada Mesin Pendingin Kompresi Uap Dengan Metode Pengujian Aktual Dan Simulasi," Jurnal Konversi Energi dan Manufaktur, pp. 74-81, 2018. https://doi.org/10.21009/jkem.5.2.3

[8] Y.-Y. Yan and T.-F. Lin, "Condensation heat transfer and pressure drop of refrigerant R-134a in a small pipe," International Journal of Heat and Mass Transfer, vol. 42, pp. 697-708, 1999. https://doi.org/10.1016/s0017-9310(98)00195-1

[9] N. Liu and J. Li, "Experimental study on condensation heat transfer of R32, R152a and R22 in horizontal minichannels," Applied Thermal Engineering, vol. 90, pp. 763–773, 2015. https://doi.org/10.1016/j.applthermaleng.2015.07.062

[10] S.-M. Kim and I. Mudawar, "Universal approach to predicting two-phase frictional pressure drop for adiabatic and condensing mini/micro-channel flows," International Journal of Heat and Mass Transfer, vol. 55, pp. 3246-3261, 2012. https://doi.org/10.1016/j.ijheatmasstransfer.2012.02.047

[11] S.-M. Kim and I. Mudawar, "Review of databases and predictive methods for heat transfer in condensing and boiling mini/micro-channel flows," International Journal of Heat and Mass Transfer, vol. 77, pp. 627-652, 2014. https://doi.org/10.1016/j.ijheatmasstransfer.2014.05.036

[12] D. Del Col, M. Bortolato, and S. Bortolin, "Comprehensive experimental investigation of two-phase heat transfer and pressure drop with propane in a minichannel," International Journal of Refrigeration, vol. 47, pp. 66-84, 2014. https://doi.org/10.1016/j.ijrefrig.2014.08.002

[13] F. C. McQuiston, J. D. Parker, J. D. Spitler, and H. Taherian, Heating, ventilating, and air conditioning: analysis and design: John Wiley & Sons, 2023.

[14] R. Eldeeb, V. Aute, and R. Radermacher, "A survey of correlations for heat transfer and pressure drop for evaporation and condensation in plate heat exchangers," International Journal of Refrigeration, vol. 65, pp. 12-26, 2016. https://doi.org/10.1016/j.ijrefrig.2015.11.013

[15] X. Tao and C. A. I. Ferreira, "Heat transfer and frictional pressure drop during condensation in plate heat exchangers: Assessment of correlations and a new method," International Journal of Heat and Mass Transfer, vol. 135, pp. 996-1012, 2019. https://doi.org/10.1016/j.ijheatmasstransfer.2019.01.132

[16] S. Marzouk, M. Abou Al-Sood, E. M. El-Said, M. K. El-Fakharany, and M. Younes, "Study of heat transfer and pressure drop for novel configurations of helical tube heat exchanger: a numerical and experimental approach: SA Marzouk et al," Journal of Thermal Analysis and Calorimetry, vol. 148, pp. 6267-6282, 2023. doi: 10.1007/s10973-023-12067-7

[17] F. Wang, G. Maidment, J. Missenden, and R. Tozer, "A novel special distributed method for dynamic refrigeration system simulation," International Journal of Refrigeration, vol. 30, pp. 887-903, 2007. https://doi.org/10.1016/j.ijrefrig.2006.10.010

[18] I. Fayssal and F. Moukalled, "A New Numerical Approach for Predicting the Two-Phase Flow of Refrigerants during Evaporation and Condensation," Numerical Heat Transfer, Part B: Fundamentals, vol. 62, pp. 341-369, 2012. https://doi.org/10.1080/10407790.2012.707009

[19] L. Zhang, J. Liu, and X. Xu, "Numerical simulation of heat transfer performance of R410A in condensing-superheated zone," International Journal of Refrigeration, vol. 128, pp. 206-217, 2021. https://doi.org/10.1016/j.ijrefrig.2021.03.019

[20] X. Jia, "A distributed model for prediction of the transient response of an evaporator," in Fuel and Energy Abstracts, 1996, p. 48. https://doi.org/10.1016/0140-7007(95)00015-4G

[21] S. Li and Y. Ju, "Numerical study on the condensation characteristics of various refrigerants outside a horizontal plain tube at low temperatures," International Journal of Thermal Sciences, vol. 176, p. 107508, 2022. doi: 10.1016/j.ijthermalsci.2022.107508

[22] M. Moradkhani, S. Hosseini, M. Song, and A. Abbaszadeh, "Reliable smart models for estimating frictional pressure drop in two-phase condensation through smooth channels of varying sizes," Scientific Reports, vol. 14, p. 10515, 2024. https://doi.org/10.1038/s41598-024-60898-7

[23] Y. Sun, H. Wang, F. Nie, M. Gong, and J. Shen, "Investigations on the heat transfer enhancement of converging minitubes for methane condensation," International Journal of Refrigeration, vol. 160, pp. 357-372, 2024. https://doi.org/10.1016/j.ijrefrig.2024.01.015

[24] O. A. Marzouk, "Condenser pressure influence on ideal steam rankine power vapor cycle using the python extension package cantera for thermodynamics," arXiv preprint arXiv:2503.00180, 2025. doi: 10.48550/arXiv.2503.00180

[25] Y. Jiang, Y. Feng, S. Tian, Z. Liu, X. Wang, Y. Wu, and Y. Zhang, "Experimental and numerical optimization of a scroll expander for small-scale ORC systems using pure and mixture working fluids," Energy, p. 137333, 2025.doi: 10.1016/j.energy.2025.137333.

[26] H. Wang and S. Touber, "Distributed and non-steady-state modelling of an air cooler," International Journal of Refrigeration, vol. 14, pp. 98-111, 1991. https://doi.org/10.1016/0140-7007(91)90082-r

[27] D. Ndiaye and M. Bernier, "Transient modeling of refrigerant-to-airfin-and-tube heat exchangers," HVAC&R Research, vol. 16, pp. 355-381, 2010. https://doi.org/10.1080/10789669.2010.10390909

[28] I. Toumi, "An upwind numerical method for two-fluid two-phase flow models," Nuclear Science and Engineering, vol. 123, pp. 147-168, 1996. https://doi.org/10.13182/nse96-a24180
[29] E. M. Smith, Advances in thermal design of heat exchangers: Wiley, 2005.
[30] M. R. Conde, A contribution to heat pump design by simulation: Verlag nicht ermittelbar, 1992.
[31] X. Jia, "A distributed model for prediction of the transient response of an evaporator," in Fuel and Energy Abstracts, 1996, p. 48. https://doi.org/10.1016/0140-7007(95)00015-4
[32] X. Jia, C. Tso, P. Jolly, and Y. Wong, "Distributed steady and dynamic modelling of dry-expansion evaporators: Modèlisation du régime stable et du régime transitoire des évaporateurs à détente sèche," International Journal of Refrigeration, vol. 22, pp. 126-136, 1999. https://doi.org/10.1016/s0140-7007(98)00043-7
[33] L. Yang and C.-L. Zhang, "Two-fluid model of refrigerant two-phase flow through short tube orifice," International Journal of Refrigeration, vol. 28, pp. 419-427, 2005. doi: 10.1016/j.ijrefrig.2004.06.007
[34] G. B. Wallis, One-Dimensional Two-Phase Flow., New York: McGraw-Hill, 1969.
[35] Y. Yao, Y. Jiang, S. Deng, and Z. Ma, "A study on the performance of the airside heat exchanger under frosting in an air source heat pump water heater/chiller unit," International Journal of Heat and Mass Transfer, vol. 47, pp. 3745-3756, 2004. https://doi.org/10.1016/j.ijheatmasstransfer.2004.03.001
[36] J. Nyers and G. Stoyan, "A dynamical model adequate for controlling the evaporator of a heat pump," International Journal of Refrigeration, vol. 17, pp. 101-108, 1994. https://doi.org/10.1016/0140-7007(94)90050-7
[37] R. A. Berry, J. W. Peterson, H. Zhang, R. C. Martineau, H. Zhao, L. Zou, D. Andrs, and J. Hansel, "RELAP-7 theory manual," Idaho National Laboratory (INL), Idaho Falls, ID (United States)2018.
[38] G. Rigot, Transmission et échangeurs de chaleur: Les Editions parisiennes, 1991.
[39] V. D. Ingenieure and V.-G. V. u. Chemieingenieurwesen, "Einführung in die Lehre von der Wärmeübertragung," in VDI-Wärmeatlas: Berechnungsblätter für den Wärmeübergang, ed: Springer, 1997, pp. 1-56. https://doi.org/10.1007/978-3-662-10745-4_1.
[40] P.-Q. Vu, K.-I. Choi, J.-T. Oh, and H. Cho, "Condensation heat transfer of R22, R410A and R32 inside a multiport mini-channel tube," 2018.
[41] W. Chen and X. Fang, "A note on the Chen correlation of saturated flow boiling heat transfer," International Journal of Refrigeration, vol. 48, pp. 100-104, 2014. https://doi.org/10.1016/j.ijrefrig.2014.09.008
[42] D. Chen and S. Lin, "Underpressure of vaporization of refrigerant R-134a through a diabatic capillary tube," International Journal of Refrigeration, vol. 24, pp. 261-271, 2001. https://doi.org/10.1016/s0140-7007(00)00019-0
[43] A. H. Fundamentals, "American society of heating," Refrigerating and Air-Conditioning Engineers, 2005.
[44] J. R. Thome, "Wolverine engineering databook III," 2006.
[45] J. C. Chen, "Correlation for boiling heat transfer to saturated fluids in convective flow," Industrial & engineering chemistry process design and development, vol. 5, pp. 322-329, 1966. https://doi.org/10.1021/i260019a023
[46] D. C. Rennels, Pipe flow: A practical and comprehensive guide: John Wiley & Sons, 2022.
[47] "Relative Roughness of Pipe," Nuclear-Power.com, Jun. 22, 2025. [Online]. Available: [https://www.nuclear-power.com/nuclear-engineering/fluid-dynamics/major-head-loss-friction-loss/relative-roughness-of-pipe/].
[48] N.-H. Kim, J.-H. Yun, and R. Webb, "Heat transfer and friction correlations for wavy plate fin-and-tube heat exchangers," 1997. https://doi.org/10.1115/1.2824141
[49] J. S. Van Der Meer, "Simulation of a refrigerant evaporator," 1989.
[50] M. O. Didi, N. Kattan, and J. Thome, "Prediction of two-phase pressure gradients of refrigerants in horizontal tubes," International Journal of Refrigeration, vol. 25, pp. 935-947, 2002. https://doi.org/10.1016/s0140-7007(01)00099-8
[51] S. M. Ghiaasiaan, Two-phase flow, boiling, and condensation: in conventional and miniature systems: Cambridge University Press, 2017. https://doi.org/10.1017/9781316597392
[52] J. R. Thome and A. Cioncolini, "Flow boiling in microchannels," in Advances in Heat Transfer. vol. 49, ed: Elsevier, 2017, pp. 157-224. https://doi.org/10.1016/bs.aiht.2017.06.001
[53] J. R. Thome and A. Cioncolini, "Two-phase pressure drop," in ENCYCLOPEDIA OF TWO-PHASE HEAT TRANSFER AND FLOW I: FUNDAMENTALS AND METHODS, ed: World Scientific, 2016, pp. 143-176. https://doi.org/10.1142/9789814623216_0023
[54] R. Radermacher and Y. Hwang, Vapor compression heat pumps with refrigerant mixtures: CRC press, 2005. https://doi.org/10.1201/9781420037579
[55] X. Boissieux, M. Heikal, and R. Johns, "Two-phase heat transfer coefficients of three HFC refrigerants inside a horizontal smooth tube, part I: evaporation," International Journal of Refrigeration, vol. 23, pp. 269-283, 2000. https://doi.org/10.1016/s0140-7007(99)00056-0